

Recent Theoretical Progress in Understanding Coherent Structures in Edge and SOL Turbulence

S. I. Krasheninnikov

University of California, San Diego, California

D. A. D'Ippolito and J. R. Myra

Lodestar Research Corporation, 2400 Central Avenue, Boulder, Colorado 80301

August, 2007; revised October, 2007
submitted to *Journal of Plasma Physics*

DOE/ER/54392-43

LRC-07-118

Lodestar Research Corporation
2400 Central Avenue, Boulder, CO 80301

Recent Theoretical Progress in Understanding Coherent Structures in Edge and SOL Turbulence*

S. I. Krasheninnikov

University of California, San Diego, California

D. A. D'Ippolito and J. R. Myra

Lodestar Research Corporation, 2400 Central Avenue, Boulder, Colorado

Abstract

This paper reviews some theoretical aspects of the dynamics of the meso-scale filaments extending along the magnetic field lines in the edge plasma, which are often called “blobs.” It starts with a brief historical survey of experimental data and the main ideas on edge and SOL plasma transport, which finally evolved into the modern paradigm of convective very-intermittent cross-field edge plasma transport. It is shown that both extensive analytic treatment and numerical simulations demonstrate that plasma blobs with enhanced pressure can be coherently convected toward the wall. The mechanism of convection is related to an effective gravity force (e.g. due to magnetic curvature effects), which causes plasma polarization and a corresponding $\mathbf{E} \times \mathbf{B}$ convection. The impacts of different effects (e.g. X-point magnetic geometry, plasma collisionality, plasma beta, etc.) on blob dynamics are considered. Theory and simulation predict, both for current tokamaks and for ITER, blob propagation speeds and cross-field sizes to be of the order of a few hundred meters per second and a centimeter respectively, which are in reasonable agreement with available experimental data. Moreover, the concept of blobs as a fundamental entity of convective transport in the SOL provides explanations for observed outwards convective transport, intermittency and non-Gaussian statistics in edge plasmas, and enhanced wall recycling in both toroidal and linear machines.

1. Introduction

It is well known that the confinement of plasma in magnetic fusion devices is determined, in large part, by turbulent plasma processes. These processes, which vary from very violent (e.g. disruption) to rather mild (as in improved confinement regimes), are very complex, and although they have been under intense experimental and theoretical studies for about a half a century, they are not well understood yet.

Detailed experimental investigations of the fundamental properties of fusion plasma turbulence started with the study of turbulence in the edge region, which bridges the hot core and material wall. The main reason for the initial attention to edge turbulence was the availability of relatively simple diagnostics. However, additional motivations came from two other observations: i) the suppression of edge turbulence results in improved confinement for the entire device, and ii) edge turbulence affects heat and particle fluxes to material walls and, therefore, is important for wall erosion and plasma contamination in both current experiments and, especially, future reactors.

The poloidal projection of different plasma regions of a diverted tokamak is shown in Fig. 1. The edge plasma occupies a part of the core, which is adjacent to the separatrix, and so-called scrape-off layer (SOL) and private regions, which both go all the way to main chamber wall and divertor targets.

As one can see from Fig. 1, the edge contains regions with both closed (inside the separatrix) magnetic field lines and open (outside separatrix) magnetic field lines, which intersect the material surfaces. In modern devices the typical edge plasma density varies from $\sim 10^{14} \text{ cm}^{-3}$ in the most inner and divertor regions, to $\sim 10^{12} \text{ cm}^{-3}$ or less at the main chamber wall, while the edge plasma temperature varies from a few hundred eV close to the core to a few eV and even sub-eV range in the divertors (although the electron and ion temperatures in the far SOL region may differ significantly). Plasma neutralization at material surfaces and volumetric recombination (in so-called detached regimes) causes neutral influx into the plasma, and

subsequent neutral ionization, which re-establishes plasma particle balance. This process is called plasma recycling. We notice that plasma and neutral particle fluxes to the surfaces also carry the heat flux and erode the surface material. Both of these effects, determining the heat removal requirements and the lifetime of the first wall are very important issues for a fusion reactor.

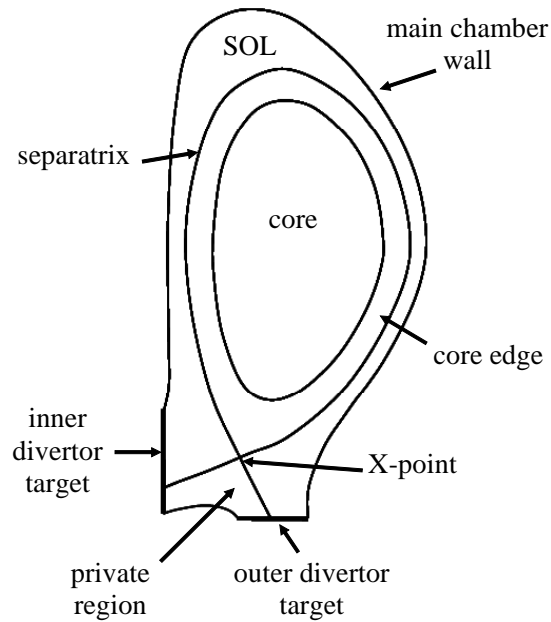


Fig. 1. Cross-section of a typical diverted tokamak showing the magnetic topology and the material boundaries surrounding the plasma.

A detailed review of the processes related to the edge plasma and neutral gas transport and interactions with material surfaces relevant for a fusion reactor can be found in Ref. [1]. An overarching physical picture of how the edge plasma “works”, which emerged in the last decade of the 20th century and seemed to be in agreement with experimental data, can be explained by the following “classical” picture. Both heat and particle fluxes are transported through the separatrix into the SOL by anomalous processes. In low confinement mode (L-mode) cross-field anomalous transport is relatively large while in high confinement mode (H-mode) it is significantly weaker. But in H-mode, the edge plasma is subject to violent events associated with destabilization of MHD modes, so-called edge-localized modes (ELMs), which are not observed

in the L-mode regimes. In the SOL, parallel heat conduction becomes very important for heat transport. It rapidly dumps heat flux, entering the SOL through the separatrix, into the cold divertor plasma, which is continuously cooled down by plasma recycling processes. As a result, practically no heat impinges onto the main chamber wall. Moreover, in some cases (specifically detached regimes) the divertor plasma may be so cold that plasma volumetrically recombines before it reaches the divertor targets (e.g. see Ref. [2] and the references therein). Both impurity radiation loss and enhancement of cross-field plasma transport in the SOL, help the transition to detachment. What is important to note about the preceding classical picture is the implicit assumption that parallel transport processes are dominant in the SOL. These parallel processes are imagined to compete with weak diffusive processes to establish a rather short radial SOL width, keeping the plasma away from the main chamber walls. In the classical picture, edge plasma parameter fluctuations caused by anomalous processes were thought not to matter much (except perhaps those caused by ELMs).

However, already early experimental studies of edge plasmas in tokamaks had already revealed rather large amplitude turbulence in the edge region (e.g. plasma density fluctuations of the order of the averaged plasma density) and an intermittent character of the turbulence. Moreover, the very first applications of fast cameras for diagnostics of edge plasma phenomena identified the existence of coherent structures [3] (see Fig. 2). Awhile later, such structures were also found with 2D probe arrays [4] and with imaging diagnostics, such as the gas-puff-imaging (GPI) systems [5] on NSTX and C-Mod (see Fig. 3).

These filamentary coherent structures extended along the magnetic field lines, often called “blobs”, were believed to be responsible for a strong intermittency of the SOL plasma turbulence observed with probes. The summaries of these initial efforts to study the edge plasma turbulence can be found in the reviews [6,7]. Further studies demonstrated that blobs are an almost ubiquitous phenomena in the edge plasmas of both tokamaks and stellarators [8], supporting earlier conclusions on the similarities of plasma edge turbulence in different toroidal magnetic devices [9]. Nevertheless, at this time, it was still not clear what role blobs played in

the overall physical picture of edge plasma transport. Even though in some experiments (e.g. Refs [10 - 12]) plasma transport enhancement in the far SOL was observed, it was neither linked directly to the blobs, nor did it alarm the edge plasma community about the possibility of enhanced plasma interactions with the main chamber wall.

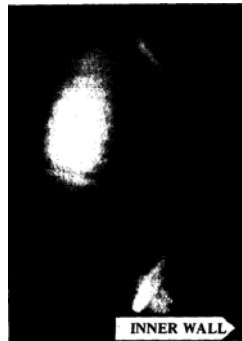


Fig. 2. Illumination from the gas puffing position in ASDEX shows coherent filamentary structures. {Figure taken from Ref. [3]}

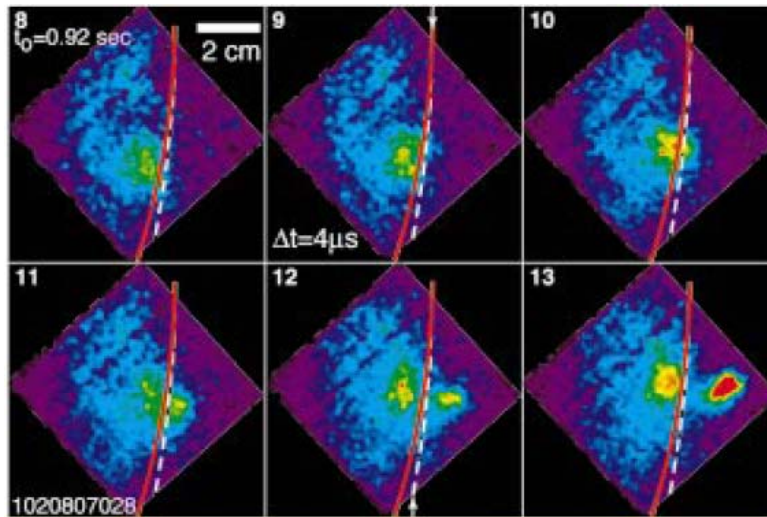


Fig. 3. Sequences of six experimental images taken at a 250 kHz frame rate, showing space and time evolution of a blob originating inside the last closed flux surface (LCFS) at the outboard SOL of C-Mod. The red line is the LCFS; the black–white line is the toroidal projection of the outboard limiter. {Figure taken from Ref. 5}

An important change in the field's overall understanding of edge transport came at the turn of the century, when analysis of experimental data from Alcator C-Mod indicated that a large fraction (~ 1) of plasma particle flux entering the SOL from the core does not flow into the divertor (as believed in the classical picture) but is instead transported radially to the main chamber wall [13]. As a result, in addition to the plasma-neutral-plasma recycling loop in the divertor, another independent recycling loop exists in the main chamber (see Fig. 4 taken from Ref. [13]).

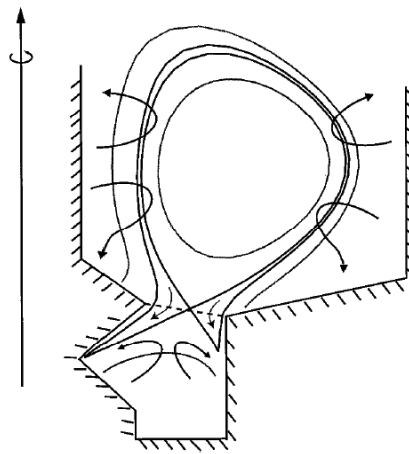


Fig. 4. Sketch showing the plasma-neutral-plasma recycling loops in the divertor region and in the main chamber. The former is due to classical parallel transport along field lines in the SOL, and the latter (main chamber recycling) is due to the edge turbulence and blob transport. {Figure taken from Ref. [13]}

Because of the fast parallel plasma transport on open field lines in the SOL, the observed large radial plasma flux to the main chamber wall requires a very large effective plasma diffusion coefficient, D_{eff} , much higher than that given by Bohm diffusion. But such a large D_{eff} , together with the fact that the D_{eff} would have to be a strongly increasing function of radial position to match the experimental data, began to cast doubt on the application of a diffusive mechanism for the description of the SOL plasma transport. Rather, it seemed to suggest that transport in edge plasmas, and in the SOL in particular, is more convective than diffusive [13]. In a paper reviewing edge plasma physics issues [14], it was suggested that “a possible explanation of the origin of this non-diffusive plasma transport can be the plasma

filamentation caused by a strong edge turbulence. The plasma filaments (strips, with extension along magnetic field less than $q\pi R$) moving in a vacuum are not confined at outer side of torus and quickly propagate all the way to the wall.”.

It was quickly realized that fast plasma transport to the main chamber wall would have important implications for the ITER design. Consequently, all these C-Mod findings triggered intensive studies of edge plasma turbulence and transport, which materialized in a large number of publications devoted to these issues. Moreover, very soon it became clear that the dynamics of plasma filaments generated by ELMs is very similar to blob dynamics (e.g. [15]), which suggests some similarities in the physics of ELM filaments and blobs.

In Refs. [16, 17] a first qualitative theory of individual blob dynamics was suggested. This theory assumes that due to some turbulent processes in the vicinity of the last closed flux surface (LCFS), a filament with large plasma density at the outer side of the torus is peeled off the bulk plasma, as sketched in Fig. 5.

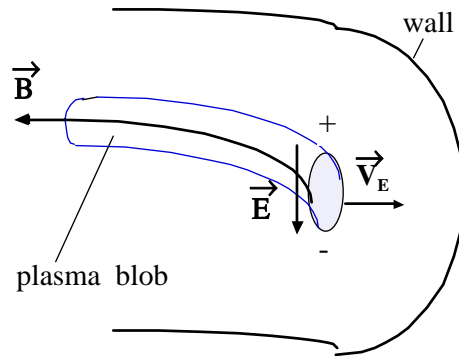


Fig. 5. Sketch of a plasma “blob” (2D) or “filament” (3D) on the outer midplane of the tokamak. This structure is localized in the plane perpendicular to the magnetic field \mathbf{B} but is extended parallel to \mathbf{B} . The outwards toroidal curvature force induces (1) an $\mathbf{F} \times \mathbf{B}$ particle drift, (2) a vertical charge polarization, (3) a vertical electric field, and (4) an outwards $\mathbf{E} \times \mathbf{B}$ drift. Any species-summed force leads to the same effects, so this is a universal transport mechanism at the boundary of a confined plasma. The blobs can originate from the nonlinear evolution of either turbulence or macroscopic MHD instabilities.

Then, plasma polarization (i.e. charge separation) caused by effective gravity drifts at the outer side of the torus (curvature and ∇B drifts in tokamaks), results in a radial $\mathbf{E} \times \mathbf{B}$ convection of

the plasma blob toward the main chamber wall. The magnitude of the electric field and, therefore, the convection speed are determined from the balance of polarization and parallel currents. In Refs. [16, 17] the blob was assumed to be in the far SOL and the parallel current to be limited by sheath “resistivity” [18, 19]. In this case, it was shown that indeed the blob can propagate as a coherent structure with a speed of the order of a few hundred meters per second, a result which was in rough agreement with then-available experimental data. Since then, the theory of blob dynamics, although still having an effective gravity as a driving mechanism, was significantly extended by incorporation of additional physics. Also, both 2D and 3D numerical simulations were very helpful in both verification of analytic results and in obtaining a better understanding of blob dynamics. Reviewing these developments is the main goal of the present paper, which significantly extends earlier surveys of blob physics [20, 21] to take into account the rapid development in this area.

From the preceding discussion it can already be seen that a paradigm which considers isolated blobs to be the fundamental entity for convective transport in the SOL is capable of (at least) qualitative agreement with experimental observations in several important respects. In particular, the blob paradigm provides:

- (1) a robust mechanism for outwards convective transport and enhanced wall recycling in both toroidal and linear machines [16, 17];
- (2) a mechanism for inward transport of impurities [22];
- (3) radial velocities of the same order of magnitude as in experiments [16, 23, 24];
- (4) two-scale (diffusive, convective) profiles of density and particle flux [17]; and,
- (5) a description that naturally incorporates intermittency and non-Gaussian statistic [see Sec. 6].

Point (2) arises from considering the propagation of density holes, for which the induced charge polarization, and hence propagation direction, is reversed from that of blobs. Point (4) follows from superposing the dominantly convective transport of blobs in the far SOL with the turbulent diffusion that is expected in the vicinity of the LCFS.

We should note here that all main ingredients of blob theory (effective gravity-driven charge separation, induced $\mathbf{E} \times \mathbf{B}$ drift, sheath-resistivity limiting the parallel current) are well known and were used in the study of SOL plasma turbulence before the publication of Refs. [16, 17]. For example, in Refs. [19, 25] it was shown that the sheath boundary conditions alter plasma stability (e.g. for the “gravitational” mode). In other papers [26-28], statistical characteristics of plasma turbulence driven by “gravitational” instability in the SOL were studied numerically and similarity with “Self Organized Criticality” (SOC) models (see Refs. [29-31]) including ballistic avalanche-type effects was found. However, only starting with Refs. [16, 17] were blobs treated as individual (coherently propagating) meso-scale structures with plasma density significantly higher than the ambient plasma; therefore, the recognition of the blob as an important nonlinear entity is not related (at least directly) to avalanche effects. In some respects, blob dynamics has more in common with the evolution of pellet clouds (e.g. see Refs. [32, 33] and the references therein).

Furthermore, while simplified (e.g. 2D) numerical models of SOL turbulence can help to shed insight into the complex processes responsible for the observed intermittent transport, the similarity of statistical properties between experimentally measured SOL turbulence and the results of 2D numerical modeling may be a bit superficial. 2D simulations, which usually only consider a part of outer side of the torus, cannot describe the effects of “good curvature” from the inner side of the torus. It is not yet clear how such 3D effects impact blob formation (which may be due to turbulent processes not related to “gravitational” drive) in the vicinity of the LCFS. What we observe in the SOL may be the result of more complex (e.g. 3D) blob formation near the LCFS acting in synergy with curvature effects, which propel blobs to the outer wall. Thus, it is useful to separate the blob formation and blob propagation aspects of SOL turbulence.

In this paper we review mainly theoretical aspects of the dynamics of an isolated blob (e.g. structural stability of the blob, impact of blob plasma parameters and geometry of magnetic field, etc.) with some experimental illustrations. Detailed discussion of the mechanisms of blob

generation are beyond the scope of this paper. Additional information and recent progress in the understanding of edge plasma turbulence can be found in Refs. [34, 35].

2. Simplified blob equations

In order to make some qualitative estimates of blob properties and dynamics we consider tractable but still physically relevant 2D models of blobs based on plasma polarization due to an effective gravity force, the physics of which was discussed in the previous Section.

We begin with the equation for charge conservation

$$-\nabla \cdot \mathbf{J}_{\perp} = \nabla_{\parallel} J_{\parallel}. \quad (1)$$

It will be seen that coherent structures like blobs emerge as the result of equilibration of plasma polarization caused, in particular, by an effective gravity force, and the dissipation of that polarization due to parallel current. A schematic illustration this physics is given in Fig. 6.

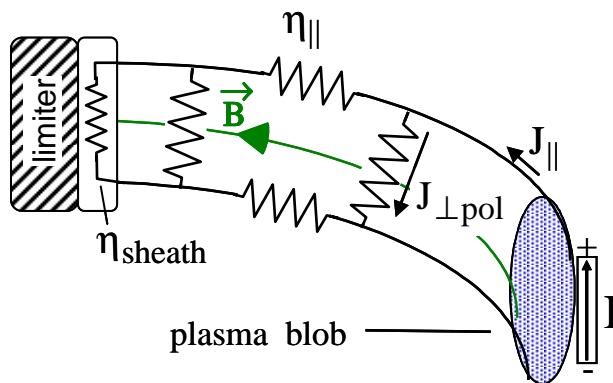


Fig. 6 Equivalent circuit and possible current paths for an enlarged view of the blob shown in Fig. 5. Note the dipole structure of the parallel current. The charge polarization from effective gravity acts as a current source I , at right. Possibilities for closure of the current loop are discussed in the text, including closure at the sheath due to the effective resistivity η_{sheath} , and closure by perpendicular ion polarization currents, $J_{\perp \text{pol}}$. The size of the various effective resistances controls the distribution of currents, as well as the total potential and therefore the blob speed $\mathbf{V}_{\mathbf{E} \times \mathbf{B}}$.

2.1 Blob polarization mechanisms

The perpendicular current can be written as the sum of the ion inertia polarization current and the current induced by the charged-particle drifts due to an arbitrary force density \mathbf{F} , which also causes blob polarization.

$$\nabla \cdot \frac{d}{dt} \left(\frac{nMc^2}{B^2} \nabla_{\perp} \Phi \right) = \nabla_{\parallel} J_{\parallel} + \frac{c}{B} \mathbf{b} \cdot \nabla \times \mathbf{F}, \quad (2)$$

where n is the plasma density, M is the ion mass, B is the magnetic field stress, $\mathbf{b} = \mathbf{B}/B$, Φ is the electrostatic potential, c is the speed of light, $d(\dots)/dt = \partial(\dots)/\partial t + \mathbf{V}_{\mathbf{E} \times \mathbf{B}} \cdot \nabla$, and $\mathbf{V}_{\mathbf{E} \times \mathbf{B}} = c(\mathbf{b} \times \nabla \Phi)/B$.

By considering different \mathbf{F} 's, the blob physics of the previous section can be easily generalized to a large number of forcing mechanisms in addition to curvature and grad-B. These include wall (e.g. divertor plate) tilt [36], neutral wind [37], centrifugal forces, perpendicular temperature gradients at a sheath interface [38, 39] and parallel shear of the $\mathbf{E} \times \mathbf{B}$ drift velocity [38]. Indeed this list contains the same forces that give rise to linear instability in the edge and SOL plasma; all that is required to drive blob propagation is a net species summed $\mathbf{b} \cdot \nabla \times \mathbf{F}$.

For the basic curvature (and grad-B) driven blobs discussed in Sec. 1, we can make the replacement

$$\frac{c}{B} \mathbf{b} \cdot \nabla \times \mathbf{F} = \frac{2c}{B} \mathbf{b} \times \mathbf{e}_x \cdot \nabla p \rightarrow \frac{2cT}{B} \mathbf{b} \times \mathbf{e}_x \cdot \nabla n \propto \frac{\partial n}{\partial y}, \quad (3)$$

where the form after the arrow \rightarrow gives the constant temperature case. Here, we consider slab geometry and assume that x and y are, respectively, local radial and poloidal coordinates, while z goes along the magnetic field. For toroidal devices, the slab model is applied on the outer midplane, with $\mathbf{R} = R\hat{\mathbf{e}}_x$ denoting the major radius of the torus. An important class of models for some forces, including curvature, yields $\mathbf{b} \cdot \nabla \times \mathbf{F} \propto \partial n / \partial y$. This arises when (i) the force density $\mathbf{F} = nm\mathbf{g}_{\text{sp}}$ where \mathbf{g}_{sp} has the interpretation of a single-particle gravitational acceleration, (ii) the force is in the radial (x) direction, and (iii) the density n varies more rapidly than \mathbf{g}_{sp} so that

$\mathbf{n}\mathbf{b}\cdot\nabla\times\mathbf{g}_{\text{sp}} \ll -\mathbf{b}\times\mathbf{g}_{\text{sp}}\cdot\nabla\mathbf{n}$. In these cases, the nonlinear propagation of density blobs is *isomorphic* to the curvature-driven case, and the blob dynamics is governed by

$$\nabla\cdot\frac{d}{dt}\left(\frac{nMc^2}{B^2}\nabla_{\perp}\Phi\right)=\nabla_{\parallel}J_{\parallel}-\frac{Mc}{B}g_{\text{sp}}\frac{\partial n}{\partial y}. \quad (4)$$

Important examples of this are: the curvature force $g_{\kappa}=2c_s^2/R$, the centrifugal force for a rotating plasmas column (of radius a) $g_{\text{cent}}=V_{\theta}^2/a$, the neutral wind force $g_{\text{nw}}=v_n v_{\text{in}}$ (where v_n and v_{in} are the effective neutral velocity and ion-neutral collision frequency), and the radial component of the expansion force due to tilted plates $g_{\text{tp}}=2c_s^2\cot\theta/L_{\parallel}$ (where $\cot\theta$ provides the radial projection of the parallel thermal force on the tilted plates). This simple form holds under some idealized assumptions. The real situation is more complicated and will be considered subsequently.

Other “forces” (i.e. driving terms in the vorticity equation) do not meet the simple criteria yielding $\mathbf{b}\cdot\nabla\times\mathbf{F}\propto\partial n/\partial y$, and the dynamics is different and generally more complicated. This category includes the cases of perpendicular temperature gradients at a sheath interface [38, 39] and parallel shear of the $\mathbf{E}\times\mathbf{B}$ drift velocity [38]. The difference in these cases is that \mathbf{g}_{sp} contains gradients (e.g. of temperature or velocity parallel shear) of the plasma quantities. Nonlinear structures (e.g. “wedges” instead of “blobs”) can propagate on a background plasma which provides these gradients. If freely propagating isolated blobs (no background plasma) are postulated, the dynamics of such terms is only effective in the presence of internal asymmetries of the blob [39]. The existence and stability of coherent nonlinear structures in this case remains a subject for future work.

Before closing this subsection, we consider the ion polarization current term in more detail. For reasons of mathematical convenience and computational efficiency, the ion polarization current has often been approximated using the so-called Boussinesque approximation, which asserts that

$$\nabla \cdot \frac{d}{dt} \left(\frac{nMc^2}{B^2} \nabla_{\perp} \Phi \right) \approx \frac{nMc^2}{B^2} \frac{d}{dt} \nabla_{\perp}^2 \Phi. \quad (5)$$

The Boussinesque approximation has a long history in the turbulence studies of incompressible fluids, and has been employed frequently in the core plasma where the relative density perturbation is small $\delta n/n \ll 1$, the plasma has no zero order electric fields, and/or the scale length of the zero order density is large, $L_n = (\nabla \ln n)^{-1} \gg L_{\Phi}$. Its justification in the context of edge plasmas is considerably more strained even when the continuity equation gives $dn/dt = 0$ to sufficient accuracy.

Although the Boussinesque approximation appears to be adequate for a qualitative model of blob dynamics, its use is particularly suspect in some applications (e.g. induced zonal flows in the edge plasma due to momentum transfer between the plasma and blobs [40]). Numerical studies [41] of single isolated blob dynamics have shown that the full ion polarization current term enhances blob coherency beyond that in the Boussinesque model.

2.2 The parallel current and closure schemes

Inherent in the blob concept is the notion of propagating filamentary objects whose dynamics is coherent and “blob-like” in the 2D plane perpendicular to \mathbf{B} . This is what makes it possible to construct 2D models of blob dynamics by invoking relatively simple models of the charge (and mass) flow in the parallel direction. Several such “closure” schemes for J_{\parallel} , dealing with different physics assumptions, have proved useful and will be considered next. The main idea of such closures is to substitute the differential operator $\nabla_{\parallel} J_{\parallel}$ with an operator that acts in the 2D plane. A general form of this closure is given by

$$\nabla_{\parallel} J_{\parallel} \rightarrow \alpha \Phi - \nu \nabla_{\perp}^2 \Phi + \mu \nabla_{\perp}^4 \Phi. \quad (6)$$

In this section, we discuss the various physical effects leading to this closure and summarize the scaling of the coefficients α , ν and μ in each case.

First, we recapitulate the results of original model of blobs [16, 17], where the blob was assumed to be in far SOL and parallel current was limited by sheath “resistivity” [18, 19]. In the sheath-connected limit we neglect plasma resistivity but take into account that the parallel current coming to the sheath at the material surface, $(J_{\parallel})_{\text{sh}} = nec_s \left(1 - e^{-e(\Phi - \Phi_f)/T}\right)$, causes the departure of electrostatic potential from its floating value $\Phi_f \approx 3T/e$. As a result, we may approximate

$$\nabla_{\parallel} J_{\parallel} \rightarrow \frac{2}{L_{\parallel}} nec_s \left(1 - e^{-e(\Phi - \Phi_f)/T}\right) \approx \frac{2ne^2 c_s (\Phi - \Phi_f)}{L_{\parallel} T}. \quad (7)$$

In the constant T model, Φ_f is just a constant reference potential and may be ignored; in general it gives rise to SOL flows, blob spin [42], and a temperature gradient drive term for blob dynamics [38, 39], related to the so-called “conducting wall” mode [43].

In the limiting case of very resistive plasma (sometimes called the inertial, hydrodynamic, or Rayleigh-Taylor limit) we can neglect parallel current and have

$$\nabla_{\parallel} J_{\parallel} \rightarrow 0. \quad (8)$$

When X-points are present, a parallel current can be dispersed in the vicinity of the X-point due to large magnetic shear [38,44-46]. Close to the X-point, the fanning geometry enhances ∇_{\perp} [47], ultimately resulting in $J_{\parallel} \rightarrow 0$ deeper into the X-point region. At a matching point near the entrance to the X-point region, we have

$$\nabla_{\parallel} J_{\parallel} \rightarrow \frac{1}{L_{\parallel}} J_{\parallel} = -\frac{ik_{\parallel} \sigma_{\parallel}}{L_{\parallel}} \Phi, \quad (9)$$

where $\sigma_{\parallel} = 1/\eta_{\parallel}$ is the parallel plasma conductivity, and we consider a WKB limit where k_{\parallel} in the X-point region can be determined from the electrostatic dispersion relation $k_{\parallel}^2 \sigma_{\parallel} + k_{\perp}^2 \sigma_{\perp} = 0$ (neglecting vacuum displacement currents). Thus in the WKB limit the current closure at an X-point is heuristically [44, 48]

$$\nabla_{\parallel} J_{\parallel} \rightarrow \frac{(\sigma_{\parallel} \sigma_{\perp})^{1/2}}{L_{\parallel} \delta_b} \Phi, \quad (10)$$

where the perpendicular plasma conductivity can come from ion polarization currents [49] or collisional electron conductivity [44, 48]. Similar results are obtained for an X-point closure model which considers matching two discrete regions [46] (e.g. midplane and X-point) instead of invoking a WKB matching. This two-region model will be discussed in detail subsequently.

As another example of a closure scheme, we consider the case of finite plasma beta of the blob-filament. In this case, the plasma response is electromagnetic since finite beta of the blobs allows the magnetic field lines to bend, leading to a perpendicular displacement by an amount $\Delta \sim L_{\parallel}^2 \beta_b / R$ even though the endpoints of the field line can be regarded as fixed. [44] Field line bending couples the physics of Alfvén wave propagation into the blob model. In this case, combining Ampere's law and the ideal Ohm's law to express J_{\parallel} in terms of A_{\parallel} , and then Φ , one obtains

$$\nabla_{\parallel} J_{\parallel} \rightarrow -\frac{2}{L_{\parallel}} \frac{c^2}{4\pi V_{A0}} \nabla_{\perp}^2 \Phi, \quad (11)$$

where we have employed $A_{\parallel} = (k_{\parallel} c / \omega) \Phi$ with $\omega / k_{\parallel} = V_{A0}$, and defined the Alfvén velocity $V_{A0} = B / (4\pi n_0 m_i)^{1/2}$. The factor of 2 comes from assuming Alfvén wave boundary conditions at both ends of the field line. In Eq. (11) V_{A0} is based on the ambient background plasma density n_0 as one follows the field line away from the blob, where the blob is assumed to have higher than ambient density over some parallel length L_{\parallel} . In the nomenclature to be introduced in Sec 5, this regime is also referred to as the RX-EM regime [45]. Interestingly, the form of the closure in Eq. (11) is the same as one obtains by considering an additional (e.g. neutral) friction force $\mathbf{F} \propto M n_0 v \mathbf{V}_{\mathbf{E} \times \mathbf{B}}$ where $M n_0 v = \text{const}$. Both outgoing Alfvén waves and explicit frictional dissipation provide an equivalent energy sink for the dynamics in the perpendicular plane. A third way to get a heuristic linear damping term of the form $\nabla_{\parallel} J_{\parallel} \rightarrow -v \nabla_{\perp}^2 \Phi$ is to take into account the parallel advection of vorticity $v_{\parallel} \nabla_{\parallel} \nabla_{\perp}^2 \Phi$ with $v \approx c_s / L_{\parallel}$ (See [50, 51] and

references therein). The parallel advection term is formally smaller than the sheath-dissipation term by $(\rho_s / \delta_b)^2$, where the blob size δ_b is typically tens of ion gyroradii ρ_s . However, heuristic arguments have been given to justify its importance at high collisionality [51]. Thus, there are several physical effects which lead to a linear damping term in the vorticity equation, and all of these have been exploited in 2D computer simulations, as discussed subsequently.

Another case is obtained by considering purely dissipative closures where, as in Eq. (8), the parallel current is not explicitly retained but one considers additional diffusion of vorticity. Effectively, one has

$$\nabla_{\parallel} J_{\parallel} \rightarrow \nabla \cdot (\mu \nabla_{\perp} \nabla_{\perp}^2 \Phi) \approx \mu \nabla_{\perp}^4 \Phi, \quad (12)$$

where the last form takes μ constant (in particular independent of density). In principle, classical viscosity will provide a term of this form, although it is usually quite small. Often, vorticity diffusion is added as an ad-hoc closure in numerical simulations [52-54] to dissipate spatial structures that are too small to be resolved. The 2D hydrodynamic cascade of vorticity to small scales that occurs when the ion polarization current term is dominant ultimately requires some form of small scale dissipation.

From the preceding discussion it is apparent that the ‘‘blob model’’ in its fullest encompasses all possible combinations of parallel current closures and driving forces. In Secs. 3 and 4, we expand upon a few specific combinations of forces and closures in more detail. Then in Sec. 5 we discuss the parameter regimes in which each type of closure is dominant.

3. Sheath-limited model of blobs

In the case where parallel current in Eq. (4) is sheath limited we can use the 2D closure in Eq. (7). In experiments, this case can correspond to blobs situated in the far SOL. Then assuming that the effective gravity is determined by the magnetic field curvature from Eq. (4, 7) we have

$$\nabla \cdot \frac{d}{dt} \left(\frac{nMc^2}{B^2} \nabla_{\perp} \Phi \right) + \frac{2c_s^2 Mc}{RB} \frac{\partial n}{\partial y} = \frac{2ne^2 c_s (\Phi - \Phi_f)}{L_{\parallel} T}, \quad (13)$$

where the electron temperature and, therefore, floating potential $\Phi_f \approx 3T/e$ are both assumed to be constant. The continuity equation is given by

$$\frac{dn}{dt} = D\nabla^2 n - \frac{n}{\tau_{\parallel}} + \xi n \quad , \quad (14)$$

where D is the plasma diffusion coefficient, $\tau_{\parallel} = L_{\parallel}/c_s$ is the sonic flow time along the field line, and $\xi n = n_0 n < \sigma v >_i$ is the ionization source term for particles. The parallel particle loss term can limit the blob lifetime. However, blob perpendicular transport dominates the parallel particle loss in Eq. (14) when $V_b \gg \Delta x / \tau_{\parallel}$, where V_b is the radial blob velocity and Δx is the radial distance of interest, e.g. the separatrix-wall separation. The role of the ionization source term was discussed in Ref. [17], where it was shown that ionization of background neutrals can sustain the blob transport against parallel particle loss, resulting in a synergy between blob transport and recycling in achieving the “main chamber recycling regime”.

Equations (13, 14) form the closed set of equations for density blob propagation. In [16] it was shown that Eqs. (13, 14) allow an exact solution in the limits $D \rightarrow 0$, $\tau_{\parallel} \rightarrow \infty$, $\xi \rightarrow 0$ (and also neglecting the ionization contributions to the vorticity equation). This solution has the form of an isolated blob of plasma density traveling in radial (x) direction with the speed V_b

$$n_b(t, x, y) = n_{(x)}(x - V_b t) \exp\left(- (y / \delta_b)^2\right), \quad (15)$$

where $n_{(x)}(x)$ is an arbitrary function, δ_b is the effective width of the blob in the poloidal (y) direction, and

$$V_b = 2c_s \left(\frac{\rho_s}{\delta_b} \right)^2 \frac{L_{\parallel}}{R}. \quad (16)$$

For $\delta_b \sim 1$ cm, $T \sim 30$ eV, $B \sim 3$ T, and $L_{\parallel}/R \sim 10$, from Eq. (16) we estimate $V_b \sim$ a few hundred meters per second, which is in approximate agreement with experimental observations (e.g. see Ref. [35] and the references therein). Assuming that spatial scales of blob in both x - and y - directions are comparable and about 1 cm, and plasma density in the blob, n_b , is of the order

of plasma density at the separatrix we find that for the DIII-D scale tokamak with $n_b \sim 3 \times 10^{13} \text{ cm}^{-3}$ and $R \sim 1.5 \text{ m}$, each blob contains about 10^{16} plasma particles. Taking into account that plasma flux through the separatrix for a DIII-D-like device is $\sim 3 \times 10^{21} \text{ s}^{-1}$, we find that in order to play a significant role in edge plasma particle transport, the blob formation frequency at a given location at the outer side of the torus should be $\gamma_b \sim 10^4 \text{ s}^{-1}$. We notice that γ_b is lower than the characteristic frequency of drift wave turbulence at the edge, which is $\sim 10^5 \text{ Hz}$. Therefore, the formation of a blob, which is due to plasma turbulent motion, should be considered as a relatively rare event.

Although the analytic solution of Eqs. (13, 14) shows that self-propelled motion of isolated plasma blobs is indeed possible, it is not, however, clear if such motion is stable or not. And this is a very important question, since we should remember that the drive of the blob motion is just the same as the drive of the gravitational plasma instability. In addition, we note that the analytic solution describes the blob propagating through the vacuum, while in experiment blobs move through some background plasma. In order to address these and other issues of blob physics, Eqs. (13, 14) were studied numerically.

The numerical evolution of seeded plasma blobs based on Eqs. (13, 14) has been studied extensively (e.g. see Refs [22, 46, 54-58]). The plasma density profile of seeded blobs was usually taken to be Gaussian (the widths in x and y directions could be different) with the magnitude of plasma density in the blob significantly higher than the background plasma density. The results of the simulations have shown that some blobs are unstable but some can propagate as coherent structures over large distances. The main controlling factor of blob stability appears to be the spatial size δ_b of the blob. Blobs with small δ_b very quickly evolve from their original Gaussian shape into a mushroom-like structure due to the Kelvin-Helmholtz instability (e.g. see Fig. 7, taken from Ref. [54]).

Blobs with large δ_b appear to be subject to the interchange instability, causing fingering effects (e.g. see Fig. 8, taken from Ref. [55]). And only blobs having δ_b in the vicinity of some particular scale δ_* coherently propagate large distances (e.g. see Fig. 9, taken from Ref. [56]).

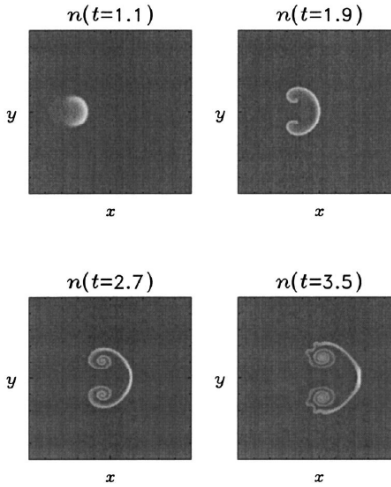


Fig. 7 Contour plot of the evolution of a two-dimensional density blob with small δ_b . During the radial motion of the blob, the density concentrates at half of its periphery creating a front. The blob is unstable to the Kelvin-Helmholtz mode and evolves to a mushroom-shaped object. {Figure taken from Ref. [54]}.

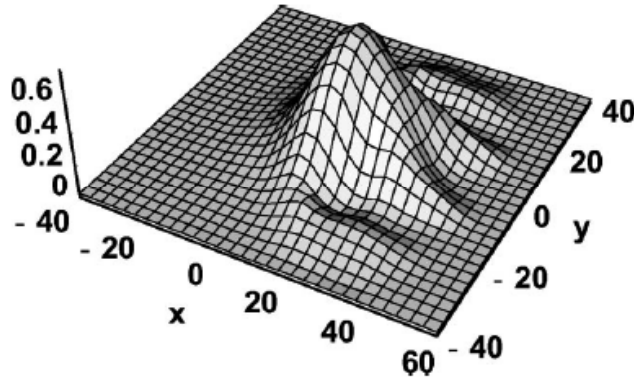


Fig. 8 Snapshot of a two-dimensional density blob with large δ_b . During the radial motion of the blob, it goes unstable to the curvature-driven interchange mode. It is shown here in nonlinear phase and the presence of radial fingers is clearly seen. {Figure taken from Ref. [55]}.

The physics of the scale δ_* can be explained from the analysis of Eq. (13). As one sees, there are three terms in that equation: the inertial term, the driving term causing plasma polarization, and the dissipation term on the right hand side. The relative magnitude of these terms depends on

δ and for $\delta_b \sim \delta_*$ they are all comparable. Normalizing the spatial coordinate and electrostatic potential to δ_* and Φ_* respectively, we find that the coefficients of all three terms in Eq. (13) become of order unity for

$$\delta_* = \rho_s \left(\frac{L_{\parallel}^2}{\rho_s R} \right)^{1/5}, \quad \frac{e\Phi_*}{T} = \left(\frac{\rho_s L_{\parallel}^3}{R^4} \right)^{1/5}, \quad V_* = c_s \left(\frac{\rho_s^2 L_{\parallel}}{R^3} \right)^{1/5}, \quad (17)$$

where V_* is the blob speed V_b from Eq. (16) for $\delta_b \sim \delta_*$.

For $\delta_b \ll \delta_*$, the dissipation term is smaller than the inertial one, and, therefore, can be ignored. As a result we arrive at the equation describing the Rayleigh–Taylor (or Richtmyer–Meshkov) instability in 2D fluid, where mushroom-like Kelvin–Helmholtz (KH) vortices are always present (e.g. see Ref. [59] and the references therein). For the case $\delta_b \gg \delta_*$ we can neglect the inertial term and come to the equation somewhat similar to that used for the description of convective turbulence of ionospheric plasmas and fluid flow in porous media (e. g. see Ref. [60] and the references therein), where fingering effects are often seen. However, in the regimes where all three terms in Eq. (13) are of the same order we can hope that mushroom and fingering effects somewhat compensate each other and we will have structurally rather stable blobs, and this is indeed what happens in the simulations.

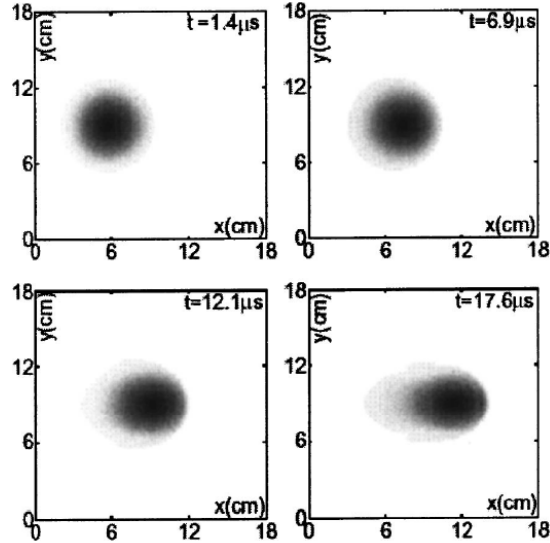


Fig. 9 Contour plot of the evolution of a two-dimensional density blob with $\delta_b \sim \delta_*$. This case is the most stable to both the Kelvin-Helmholtz and interchange modes, and the blob propagates with a minimum of distortion. {Figure taken from Ref. [56]}.

While the blob moves, the density profile evolves into a specific shape with a sharp front and a relatively long tail (e.g. see Fig. 10, taken from Ref. [57]).

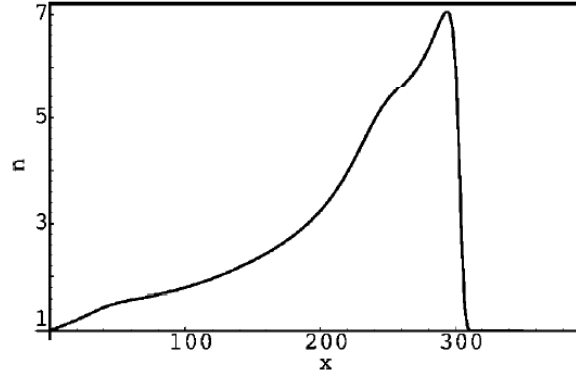


Fig. 10 Radial profile of a density blob with $D/D_* \sim 10^{-2}$. The front of the blob steepens, forming a “shock front” as it propagates, and the blob leaves behind a long density tail. This shape is observed in all simulations of blob propagation and agrees with experimental data obtained with probes (see Fig. 11). {Figure taken from Ref. [57]}

We notice that such a shape is usually observed in experimental studies, where the blob plasma density is measured with probes (e.g. see Fig. 11, taken from Refs. [61, 62]). In numerical simulations, the width of the front is determined by the magnitude of the plasma diffusion coefficient, which is usually are taken to be rather small, $D/D_* \sim 10^{-2 \div 3}$, where $D_* = V_* \delta_*$, so that an impact of diffusion processes on the overall evolution of blob is not important.

A numerical study of the impact of an external layer of sheared electric field on blob propagation [56] shows that a relatively large biasing potential Φ_{bias}

$$e\Phi_{\text{bias}}/T > (\Delta_{\text{bias}}/\rho_s)^3 \left(\rho_s^4 / RL_{\parallel}^3 \right)^{1/5}, \quad (18)$$

destroys blobs with $\delta_b \sim \delta_*$, where Δ_{bias} is the width of biased layer.

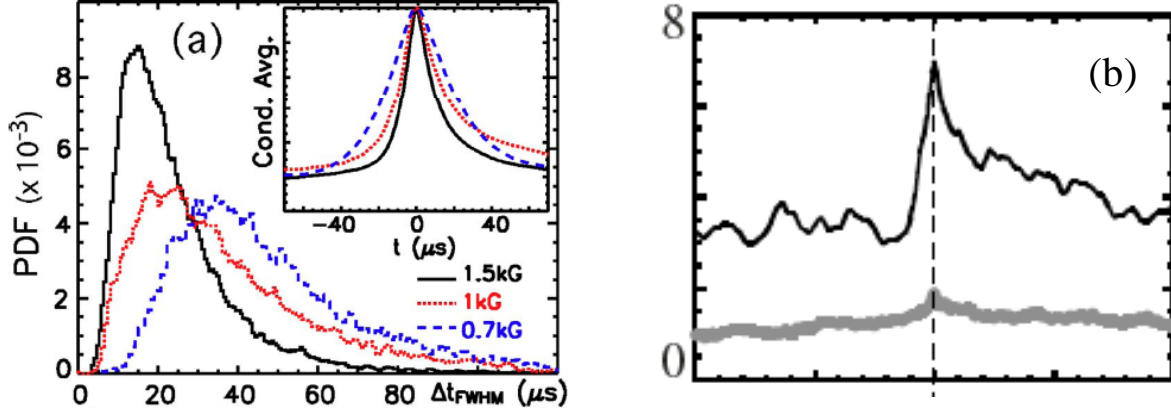


Fig 11 (a) PDF of blob event time width for three values of the magnetic field on the LAPD experiment. The insets are conditionally-averaged blob events for the three magnetic field values. (b) Time history of the conditionally-averaged probe data on DIII-D (covering a total duration of 200 μs) for two values of the plasma current: lower I_p (black curve) and higher I_p (gray curve). In each experiment, and for all values of the parameters, note the fast rise and slow decay of the signal as the blob passes the probe. {Figure adapted from Refs. [63, 64]}

In addition to blobs having increased plasma density, experiments also show the existence of plasma density holes with reduced density propagating towards the core (e.g. see Ref. [62,65]). Numerical simulation of the holes with Eqs. (13, 14) show that, in agreement with both theoretical expectations and experimental observations, holes propagate against the effective gravity and their dynamics are similar to that of blobs having plasma density comparable to the background plasma density.

So far, we have assumed that the electron plasma temperature is constant. However, since blobs are formed close to the separatrix and then move toward the wall, they are supposed to have a plasma temperature somewhat higher than the background plasma temperature. As a result, the floating potential Φ_f , which is proportional to the electron temperature within the blob, will be higher than that in the vicinity. This produces a radial electric field causing the blob plasma to spin with the frequency $\Omega_{\text{spin}} \sim (\Delta T/T_{\text{bg}}) (c_s \rho_s / \delta_b^2)$, where ΔT is the temperature difference between the blob and background plasmas, and T_{bg} is the background temperature. However, fast blob spinning will reduce the charge separation imposed by effective gravity and, therefore, decrease the poloidal electric field and slow down the radial blob motion

[42]. In order to estimate the effect of the spin, we need to compare Ω_{spin} with the effective rate of charge separation dissipation due to current through the sheath, v_{sheath} . From Eq. (13) we find $v_{\text{sheath}} \sim (c_s/L_{\parallel})(\delta_b/\rho_s)^2$. Blob spin will not affect plasma charging when $\Omega_{\text{spin}} < v_{\text{sheath}}$; in this case, the main charge dissipation mechanism is the current through the sheath, and the blob velocity estimate in Eq. (16) holds. The inequality $\Omega_{\text{spin}} < v_{\text{sheath}}$ gives the following restriction $\Delta T/T_{\text{bg}} < \delta_b^4/\rho_s^3 L_{\parallel}$, which for $\delta_b \sim \delta_*$ reduces to

$$\frac{\Delta T}{T_{\text{bg}}} < \left(\frac{\Delta T}{T_{\text{bg}}} \right)_{\text{crit}} \equiv \left(\frac{\rho_s L_{\parallel}^3}{R^4} \right)^{1/5}. \quad (19)$$

For $\Delta T/T_{\text{bg}} > \left(\Delta T/T_{\text{bg}} \right)_{\text{crit}}$ blob spinning starts to play a major role in setting the charge separation and drastically reduces radial blob plasma speed [42]. We notice that in practice the parameter $\left(\rho_s L_{\parallel}^3 / R^4 \right)^{1/5}$ is close to unity so that the inequality (19) does not pose very severe restrictions on the blob plasma parameters. This physical picture describing the impact of the plasma temperature inhomogeneity on blob dynamics was confirmed by both analytic solutions and numerical simulations [42]. In addition to the reduction of the radial blob velocity, blob spinning can also cause rotational and Kelvin–Helmholtz instabilities leading to the break up of the blob [66].

The preceding sheath closure models focus on describing the 2D structure and nonlinear dynamics of blob filaments in the perpendicular plane. However, these simple models cannot describe the full effects of realistic tokamak magnetic geometry. The effect of magnetic geometry on the filament can be treated in the interchange limit, where the blob parameters are roughly constant along B , by an appropriate field-line average [39]. In this case, motion of the filament in the normal and geodesic directions is governed by pressure-weighted $\int ds/B^2$ averages of $\nabla \ln B$ in these directions respectively. Other effects of magnetic geometry, in particular due to X-points, can result in parallel structural changes in the blob itself, considered next.

4. Other Blob Closures

Having now reviewed the physics of sheath-connected blobs in some detail, in this section we consider a few of the other possible closures mentioned in Sec. 2 and their consequences for blob propagation.

4.1 Current closure at an X-point

Since X-point (i.e. single or double null) magnetic geometry is common in modern tokamaks, it is important to understand the implications of this geometry for blob transport. Near an X-point, the local magnetic shear becomes large and the poloidal field becomes small, $B_\theta \rightarrow 0$ with the result that the magnetic flux tube is stretched into a thin elliptical fan [47], as shown in Fig. 12. This results in short scale lengths perpendicular to \mathbf{B} , enhanced cross-field polarization currents (from the $\nabla_\perp^2 \Phi$ term in the vorticity equation) and an increased role for magnetic diffusion ($\propto \eta_\parallel \nabla_\perp^2 A_\parallel$) for electromagnetic modes in a resistive plasma. Intuitively, it becomes easier for cross-field currents to flow, since they can flow across the thin direction of the fans. An X-point thus causes the current loops in Fig. 6 to close before reaching the sheaths, effectively short-circuiting them. The cross-field currents can be either ion polarization currents [45,46,49] or collisional currents due to electrons whose $\mathbf{E} \times \mathbf{B}$ conductivity is not ion-compensated in the $k_\perp \rho_i \gg 1$ limit where the ions are effectively immobile [21, 44, 48].

In the language of linear wave theory, X-points make \mathbf{k}_\perp a strong function of the coordinate along \mathbf{B} . When $k_\perp \rho_i$ becomes sufficiently large, the perturbation decays rapidly and the mode electrically *disconnects* along \mathbf{B} , i.e. a main-chamber driven mode disconnects from the divertor legs, and visa-versa. This physics gives rise to the “resistive X-point (RX) modes” [67-69], extending between the outer midplane and the X-point, and to the “divertor leg” instabilities [48] localized between the X-point and the divertor plates. Recently, analytic theories of these X-point and divertor leg modes have been developed in various approximations and applied to understand blob transport [36, 39, 44-46] using a heuristic X-point BC first proposed in Ref. [48]. These approximations rely on the rapid evanescence of the mode (blob) along \mathbf{B} as the X-point

region is encountered, which suggests the use of a WKB-like outgoing-evanescent wave boundary condition as a closure relation.

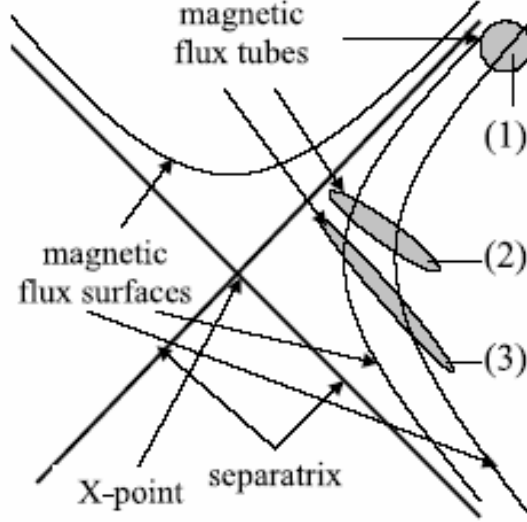


Fig. 12 Elliptical distortion of a flux tube as it passes close to an X-point. The points labeled (1), (2), (3) correspond to different toroidal locations, and flux tube is taken to be nearly circular at the outboard midplane, (1). {Figure taken from Ref. [44]}.

Employing Eq. (10), the vorticity equation in the X-point closure model is heuristically

$$\frac{(\sigma_{\parallel}\sigma_{\perp})^{1/2}}{L_{\parallel}\delta_b}\Phi \approx \frac{Mc}{B}g_{sp}\frac{\partial n}{\partial y}. \quad (20)$$

Here $\sigma_{\parallel}^{-1} = \eta_{\parallel}$ is the usual Spitzer parallel resistivity, $\sigma_{\perp} = \sigma_{\perp\text{pol}} = c^2\gamma/4\pi V_A^2$ for ion polarization current, or $\sigma_{\perp} = \sigma_{\perp v} = \omega_{pe}^2 v_e / (4\pi\Omega_e^2)$ for cross-field collisional electron conductivity.

For very small scale blobs, the vorticity advection term [not shown explicitly in Eq. (20)] $\propto 1/\delta_b^4$ will always dominate. For larger blobs, when the X-point closure term dominates, the convective blob velocity scales as $v_{E\times B} \sim \Phi/\delta_b \propto g_{sp}/(\delta_b\sigma_{\perp}^{1/2})$. From this, (and using $\sigma_{\perp\text{pol}} \propto v_{E\times B}/\delta_b$) it can easily be seen that the velocity scales with blob size as $v_{E\times B} \propto g_{sp}^{2/3}/\delta_b^{1/3}$ for ion polarization current [45], or $v_{E\times B} \propto g_{sp}/\delta_b$ for cross-field collisional electron conductivity [38, 44].

One deficiency of the WKB outgoing-evanescent closure is that it cannot provide a description of the transition from the X-point disconnected limit to the interchange (sheath-connected) limit. For this and other reasons, an electrostatic two-region model has been proposed and studied [46]. The two-region model couples two planes perpendicular to \mathbf{B} (typically midplane and divertor leg) at different points along a field line by implementing field line mapping according to the transformation provided by the magnetic geometry. In this way, two sets of continuity and vorticity equations similar to Eqs. (13, 14) of Sec. 3 are solved. The current flow between regions is governed by the parallel plasma resistivity. The two-region model delineates the boundaries between disconnected and connected modes in X-point geometry, and can assess the role of X-point-enhanced inertia (ion polarization current) on interchange modes. (In contrast, the magnetic geometry does not enter explicitly in the WKB X-point closure model.) Details are given in Ref. [46]. Here we note that if X-point effects are characterized by the ratio of perpendicular scale lengths in the two regions $\varepsilon_x \sim k_{\perp 1} / k_{\perp 2} \ll 1$ (related to the ellipticity of the fan-shaped flux tubes), then the familiar sheath-connected limit discussed in Sec. 3 occurs when $\delta_b \varepsilon_x^{2/5} > \delta_*$, which generalizes the condition $\delta_b > \delta_*$ discussed in Sec. 3.

The collisionality dependence of the blob velocity scaling was also demonstrated numerically in the two-region model, as summarized in Fig. 13. Here, the dimensionless parameters characterizing collisionality and scale size are

$$\Lambda = \frac{v_{ei} L_{\parallel}}{\Omega_e \rho_s} \quad , \quad (21)$$

$$\Theta = \hat{\delta}^{5/2} \quad , \quad (22)$$

$$\hat{\delta} = \frac{\delta_b}{\delta_*} \quad . \quad (23)$$

The parameter Λ is proportional to the resistivity impeding parallel current flow into the divertor region and is a ratio of the volume resistivity of the plasma to the effective sheath resistivity. In Eq. (23) the blob size δ_b is normalized to δ_* , the scale size at which the inertial, curvature and sheath terms are all comparable in the vorticity equation for the case of no X-point geometric effects. Note in Fig. 13 that there is a general increase of blob speed with collisionality, and that at low collisionality the smallest blobs move the fastest, while at high collisionality the reverse is true. This is in accord with the expected asymptotic analytical scalings [45,46]. Note also that very large collisionality is required to attain the asymptotic high collisionality limit for the modest value of $\varepsilon_x = 0.25$ chosen here. As most tokamak experiments lie in the range $\Lambda < 1$, the inertial or resistive ballooning closure of Eq. (8) is not generally applicable, and one of the X-point closures of this section is usually more realistic. We will return to the question of appropriate blob regimes in Sec. 5.2.

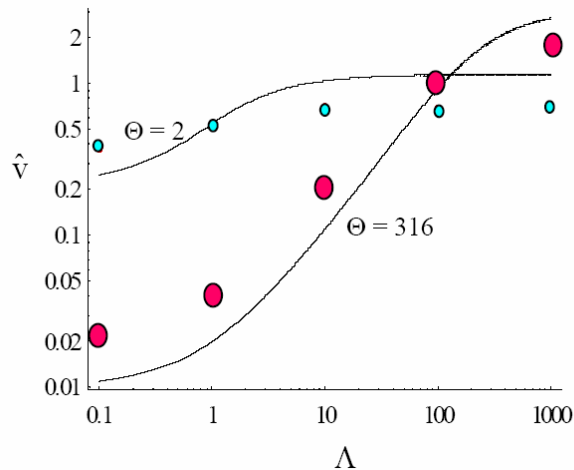


Fig. 13 Normalized radial blob velocity as a function of collisionality parameter Λ for blobs of two different sizes: $\Theta = 2$ ($\hat{\delta} = 1.3$, small dots) and $\Theta = 316$ ($\hat{\delta} = 10$, large dots) and $\varepsilon_x = 0.25$. [see Eqs. (21-23)] The dots were obtained by measuring the blob velocities from the numerical simulation. The solid curves are from an analytical blob “dispersion relation”. {Figure taken from Ref. [46] }

4.2 High-beta blobs and ELMs

Another closure limit occurs when the plasma beta of the blob, $\beta_b = 8\pi nT/B^2$, is large enough to cause field-line bending. This becomes a relevant limit when considering the propagation of ELMs in the SOL. For a hot dense ELM, the field line displacement $\Delta \sim L_{\parallel}^2 \beta_b / R$ can compete with other relevant perpendicular scales (see Fig. 14).

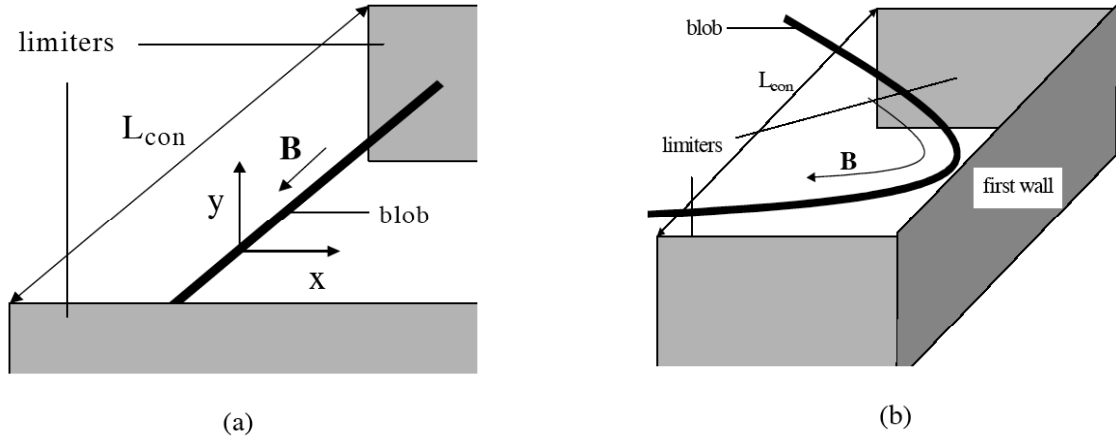


Fig. 14 Schematic illustration of the comparison of sheath connected blobs and high-beta blobs which induce field line bending. {Figure taken from Ref. [41]}

As discussed in Sec. 2, the physics of field line bending is related to the emission of Alfvén waves along the field line. A model that has been discussed in the context of pellet clouds [32, 33], blobs [44], and electromagnetic instabilities [45] is to apply an outgoing Alfvén wave condition along \mathbf{B} for the closure relation. Mathematically, the WKB outgoing wave condition means that the blob dynamics at the midplane has no knowledge of the conditions far away along the field line. Physically, the blob β_b is strong enough to drag and bend the magnetic field line with it as it convects radially. In this limit the vorticity equation becomes heuristically

$$\frac{2}{L_{\parallel}} \frac{c^2}{4\pi V_{A0}} \nabla_{\perp}^2 \Phi \approx \frac{Mc}{B} g_{sp} \frac{\partial n}{\partial y}. \quad (24)$$

where we estimate $d/dt \sim V_{A0}/(L_{\parallel}/2)$ and again we assume that the blob has a sufficiently large scale size (or sufficiently slow time scale) that the ion polarization current (vorticity advection)

term can be dropped. In the high-beta closure, the convective blob velocity scales as $v_{E \times B} \sim \Phi / \delta_b \propto g_{sp}$ independent of δ_b . The dynamical evolution of a high-beta blob has been studied numerically in Ref. [41] and is illustrated in Fig 15. Compared with sheath-connected blobs, the dynamical evolution is different [41] because of the appearance of $\nabla^2 \Phi$ rather than Φ on the LHS of Eq. (24). This tends to smooth the blob as it propagates and helps to mitigate blob internal instabilities (Kelvin-Helmholtz instability for small δ_b and curvature-driven fingering at the leading edge for large δ_b).

Because the high-beta WKB closure isolates the blob dynamics from the downstream field line plasma, the same physical regime occurs when the electrostatic X-point closure of Eq. (20) is extended electromagnetically to finite beta [45]. This limit, called the resistive-X-point electromagnetic (RX-EM) regime is identical to the high-beta regime and joins smoothly to the electrostatic X-point (RX-ES) regime. The location of these regimes is considered later.

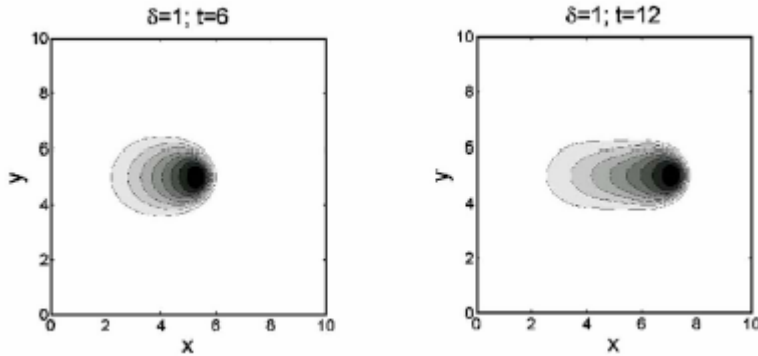


Fig. 15 High-beta blob motion for $\hat{\delta} \equiv \delta_b / \delta_* = 1$ at two different normalized times. The propagation of these blobs are different from the sheath-connected blobs, showing less tendency to develop a mushroom shape or fingering. {Figure taken from Ref. [41]}

In addition to high β_b , another feature that distinguishes ELMs from blobs is that the ELMs can carry significant unidirectional parallel plasma current convected outwards from the bulk plasma current carried in the ELM formation zone. (This unidirectional parallel plasma current is not to be confused with the dipole J_{\parallel} that arises in response to charge separation forces.) This current adds additional magneto-static $\mathbf{J} \times \mathbf{B}$ forces to the dynamics of ELMs. Preliminary studies of these effects have been reported [70], where it is shown that the currents

increase the ELM / blob coherency in the 2D plane (due to mutual attraction of adjacent current filaments). This unidirectional parallel plasma current also causes repulsive interactions with its image (either due to proximity to a conducting first wall, or to its “hole” where it leaves the ELM formation zone).

4.3 Divertor-localized blobs and the effect of wall tilt

The preceding sections have implicitly concentrated on main-chamber blobs whose drive terms come from curvature at the outboard midplane. We have noted that the geometry of the X-point electrically disconnects the midplane and divertor leg regions. Such disconnection can be expected to result in a decorrelation of the turbulence in the two regions that has been observed in numerical simulations [49, 71-74].

This same disconnection phenomenon has been employed to study divertor-localized blobs, which can be driven both by local curvature (analogous to the midplane case), and by the effect of wall tilt. [36] Wall tilt, which occurs when the surface normal to the divertor plate is not parallel to the poloidal magnetic field, introduces several interesting new features into the SOL instability and blob propagation problems. Neglecting the effect of temperature gradients on the sheath boundary condition, divertor localized blobs are approximately described by a vorticity equation of the form

$$\frac{\Phi}{L_{\parallel}} \left(\frac{\sqrt{\sigma_{\parallel}\sigma_{\perp}}}{\delta_b} + \frac{ne^2c_s}{T} \right) \approx \frac{Mc}{B} g_{sp} \frac{\partial n}{\partial y} \quad (25)$$

where

$$g_{sp} \equiv c_s^2 \left(\frac{1}{R} + \frac{\tan \alpha}{2L_{\parallel}} \right) \quad (26)$$

Here we drop the vorticity advection term on the LHS, which can describe transiently the acceleration of a blob initialized from rest. The terms on the LHS of Eq. (25) describe the

parallel current closures at each end of the field line (i.e. due to X-point and sheath boundary conditions, respectively) and L_{\parallel} is the length of the field line between the plates and the X-point region. The effective gravity term in Eq. (26) includes both curvature and tilted wall contributions. Here, α is the angle between the normal to the plate (facing outwards towards the plasma) and the poloidal magnetic field; the angle α is positive when the normal is directed outward from the poloidal field line. Thus positive (negative) tilt leads to increased (decreased) radial acceleration. [36]

Divertor-localized blobs, divertor instabilities, and other forms of divertor-induced convection [48, 74] are of particular interest because they have the potential of broadening the local divertor SOL (distributing the heat load) without impacting the confinement of the main-chamber SOL or edge plasmas.

Based on linear instability studies in the divertor region [48, 74, 75], a number of instabilities exist in a more complete model which includes temperature gradients and electromagnetic effects in the presence of wall tilt. The nonlinear implications of these effects for blob formation remain to be studied, but may be inferred heuristically from the correspondence rule discussed in Sec. 5.

5. Blob regimes and the correspondence principle

As is evident from the preceding discussion, many of the closures for $\nabla_{\parallel} J_{\parallel}$ can be understood from linear theory, since the treatment of the parallel current is usually unrelated to the convective $\mathbf{v}_{E \times B} \cdot \nabla$ nonlinearities important for blob transport. This leads to a “correspondence principle” between the linear instability and nonlinear blob transport regimes. In this section, the correspondence principle is used to construct regime diagrams, which help to unify the discussion and to indicate what parameter ranges correspond to each closure.

5.1 Correspondence between blob transport and linear instability theory

Since the fundamental physics behind blob convection in the SOL is closely related to SOL mechanisms for linear instability (consider, for example, effective gravity from curvature, sheath conductivity etc.) it is useful to keep in mind the following “*blob correspondence principle*” [45] relating the properties of the associated linear instability to the radial blob velocity and scale size:

$$\gamma \rightarrow \frac{v_x}{\delta_b}, k_{\perp} \rightarrow \frac{1}{\delta_b}, L_n \rightarrow \delta_b, k_{\parallel} \rightarrow \frac{1}{L_{\parallel}} . \quad (27)$$

Here, $\gamma = \text{Im}[\omega]$ is the growth rate of the instability, k_{\perp} is the perpendicular wavenumber, L_n is the density gradient scale length, δ_b is the perpendicular dimension (radius) of the blob, and L_{\parallel} is the blob’s filamentary length along the magnetic field. Thus it is possible to use linear instability results together with Eq. (27) to obtain heuristic closure relations for $\nabla_{\parallel} J_{\parallel}$ and, in fact, estimates of the blob convection velocity [45]. Note that the relation $\gamma \rightarrow v_x / \delta_b$, obtained by balancing $\partial / \partial t$ with $\mathbf{v}_{E \times B} \cdot \nabla$ is consistent with the notion of a coherently convecting object for which $d / dt \approx 0$.

The correspondence rule in Eq. (27) suggests that nonlinear properties of turbulent transport can be inferred from linear ones. This connection was noted qualitatively in [76] for sheath-interchange modes; Eq. (27) makes the correspondence explicit and generalizes it to more collisional regimes. Also it should be emphasized that this principle assumes that the radial transport is convective ($\Gamma = n v_x \sim n \gamma / k$) rather than diffusive ($\Gamma = D \nabla_x n \sim n \gamma / k^2 L_x$), so it applies in the spatial regions where the blob transport dominates the turbulent diffusion.

5.2 Blob regimes

The scaling of blob velocity with plasma parameters and blob size δ_b has been discussed in several recent papers [21, 45, 46, 77], where it was shown that the scaling depends on the parameter regime. Some of these regimes have been treated in the preceding sections, and the

interested reader is referred to the references for more details. Diagrams are useful to visualize how the parameter regimes fit together, and in what parameter ranges the various scalings are applicable. Here we summarize some of the results (without derivation). It is convenient to employ the linear-mode blob correspondence relation (Sec. 5.1) to understand heuristically the various regimes of blob transport.

A useful parameter space for understanding main chamber disconnected blobs (i.e. blobs that are electrically disconnected from the divertor sheaths) is shown in Fig. 16.

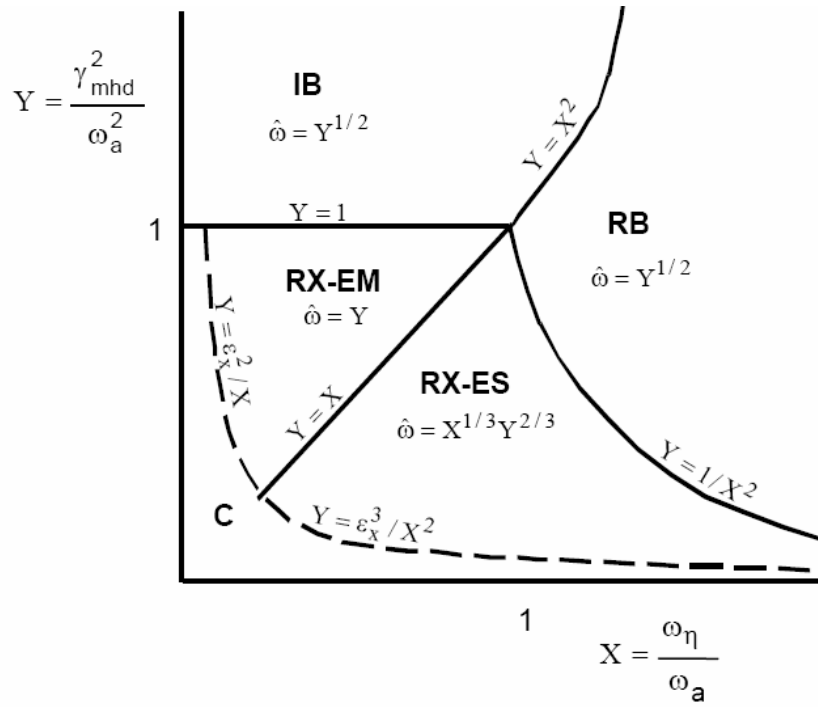


Fig. 16 Instability and blob transport regime diagram (WKB limit) with $\hat{\omega} = \gamma / \omega_a$. {Figure taken from Ref. [45]}

The characteristic frequencies in the model [45] are $\omega_\eta = \eta_\parallel k_\perp^2 c^2 / 4\pi$, $\omega_a = k_\parallel V_A$ and $\gamma_{\text{mhd}}^2 = c_s^2 / (RL_n)$. The system can be characterized by two dimensionless parameters: $X = \omega_\eta / \omega_a$, describing collisionality and scale size, and $Y = (\gamma_{\text{mhd}} / \omega_a)^2$, representing the strength of the magnetic curvature, which drives both the linear instability and the blob motion. Balancing the terms in the blob model (or linear dispersion relation) two at a time, one obtains a

number of regimes in X-Y space illustrated in Fig. 16, where the dimensionless growth rate is defined as $\hat{\omega} = \gamma / \omega_a$. The blob velocity in dimensional units is therefore $v_{E \times B} \sim k_{\perp} \gamma \sim \hat{\omega} (\omega_a / \delta_b)$.

In this figure, “IB” labels the *ideal ballooning regime* in which the curvature drive is balanced by the inertia (i.e. polarization current) so that $\omega \sim \gamma_{\text{MHD}}$. This regime generally requires that the plasma blob exceed the critical beta for ideal ballooning instability, and corresponds to a standing Alfvén wave. The label “RB” denotes the *resistive ballooning regime* in which a similar balancing occurs, but resistivity dominates line bending in the inertial term ($\omega_a^2 \ll \omega_{\eta} \gamma_{\text{mhd}}$). This regime corresponds to the inertial, hydrodynamic, or Rayleigh-Taylor closure given in Eq. (8). The labels “RX-ES” and “RX-EM” indicate the electrostatic and electromagnetic (high-beta) branches of the *resistive X-point modes*, respectively, in which the midplane curvature drive is balanced by the parallel current term in the X-point region, which either leads to evanescence or outgoing Alfvén waves. These regimes correspond to Eqs. (20) and (24), respectively, using the $\sigma_{\perp \text{pol}}$ forms. Note that the scalings for the growth rates in each regime connect smoothly across the boundaries. More details on the physics of these regimes is contained in the original reference [45]. The diagram shows, not surprisingly, that electromagnetic effects become increasingly important for large $\gamma_{\text{mhd}} / \omega_a$ (large driving force) while resistive effects dominate at large ω_{η} / ω_a (small scale sizes and/or large η_{\parallel}). Sheath-connected blobs (modes), labeled “C” in the figure are favored in the opposite limit, i.e. small $\gamma_{\text{mhd}} / \omega_a$ and ω_{η} / ω_a .

Scalings inside the sheath-connected regime “C” in Fig. 16 cannot be properly described by WKB closures, and are not uniquely represented in the “(X, Y)” parameter space. However, a different parameter space describing the connected and disconnected modes in the electrostatic limit is available using the two-region model. Results adapted from [46] are shown in Fig. 17. The normalized velocity employed in Fig. 17 is defined by

$$\hat{v} = v_x / v_*$$

$$v_* = c_s \left(\frac{\delta_*}{R} \right)^{1/2}, \quad (28)$$

The midplane and divertor regions are *disconnected* in the resistive X-point (RX) and resistive ballooning (RB) regimes (see also Fig. 16), and *connected* in the C_s and C_i regimes which occur for small collisionality and/or sufficiently large scale size, depending on the “fanning” parameter ϵ_x . The C_s regime corresponds to the sheath-connected limit of Sec. 3. The C_i regime is also a flute-interchange limit but one in which the current source (from curvature) is balance by fanning-enhanced inertia in the divertor region, rather than current to the sheaths. Typical SOL parameters for tokamak experiments put the blobs in the $\Lambda < 1$ part of the diagram, spanning the RX and C_i/C_s regimes. (see, for example, Ref. [40])

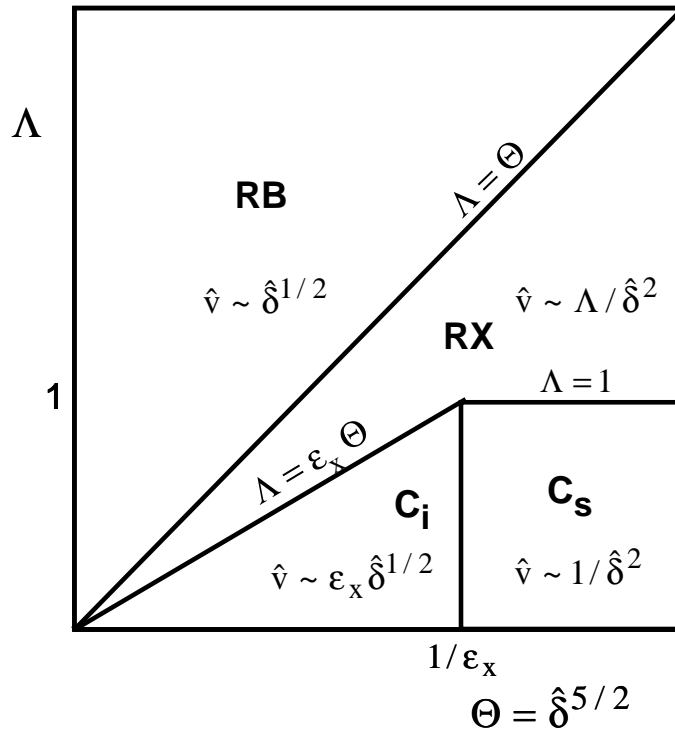


Fig. 17 Regime diagram for the electrostatic two-region model in the space of normalized collisionality Λ and scale size Θ as defined in Eqs. (21, 22). The dimensionless blob speed v and size δ are defined in Eqs. (28) {Figure adapted from Ref. [46]}

An important result from the electrostatic regime analysis is that it allows simple analytical bounds to be placed on the blob convective velocity. The small- and large- Λ limits give lower (sheath-connected) and upper (resistive ballooning) bounds, respectively, which can be put in the form

$$\frac{1}{\hat{\delta}^2} < \hat{v} < \hat{\delta}^{1/2} \quad , \quad (29)$$

or, in dimensional units

$$\frac{L_{\parallel} \rho_s^2 c_s}{R \delta_b^2} < v_x < \frac{\delta_b^{1/2} c_s}{R^{1/2}} \quad . \quad (30)$$

For typical numbers, Eq. (29) predicts v_x/c_s to be 1% or less at the lower bound and up to 10% or so at the upper bound; however, as we have noted the parameters required to attain the upper bound (RB regime) are usually not realistic in the tokamak SOL. Results of order of a few percent are characteristic of experimental measurements [65, 78, 79].

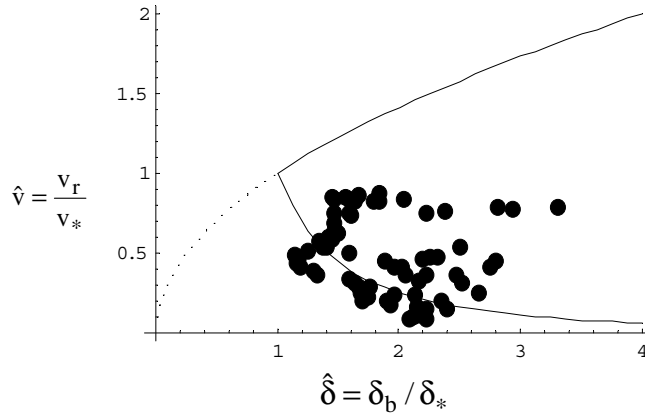


Fig. 18 Observed radial blob velocities (filled circles) in dimensionless parameter space of velocity and blob scale size. The data is approximately bounded by the theoretically predicted minimum and maximum velocities in Eq. (29) (solid lines). {Figure taken from Ref. [40]}

As illustrated in Fig. 18, Eq. (29) gives reasonable agreement with an analysis of gas-puff-imaging (GPI) data on NSTX [24, 40], in which individual blobs were tracked and their velocities calculated from successive frames. It is interesting to note that the experimental points

do not approach the upper RB boundary, but rather appear to be limited by $\hat{v} < 1$, independent of $\hat{\delta}$, which is suggestive of electromagnetic “high-beta” or “RX-EM” blob scaling from Eq. (24). For this data $v_{\text{RX-EM}} / v_* \sim L_{\parallel}^{4/5} \beta_b^{1/2} / (R \rho_s)^{2/5} \sim 0.2 - 1$.

It will be evident by now that the topic of blob regimes is rather complicated, even for the blob filaments of interest at the outboard midplane. Figures 16 and 17 do not attempt to describe the divertor localized blobs discussed in Sec. 4.3, although analogous regimes exist, in addition to new regimes introduced by wall tilt. One interesting case, relevant to divertor blobs but absent in the midplane blob analysis, is the when one end of the filament is anchored at the divertor plate while the other end is disconnected by X-point effects. In this case, it can be shown [39] that the blob velocity is of order $v \sim \omega_{\eta} c_s^2 / (\omega_a^2 R)$ under the condition that $\omega_{\eta} \gamma_{\text{mhd}} < \omega_a^2$. In Fig. 16, this would correspond to $\hat{\omega} \sim XY$ for $Y < 1/X^2$ (which would be in the RX-ES regime for a midplane centered un-anchored blob).

6. Discussion

In this section, we discuss the role of blobs in turbulence simulations and some additional transport issues. A detailed review of work on edge turbulence simulations is beyond the scope of this paper, but some references to current work are given. We also summarize some outstanding questions for future work.

6.1 Edge turbulence and blob generation

So far we have considered reduced models describing dynamics of individual blobs. Although such models help to identify the physics ingredients and parametric dependences, some other fundamental issues remain to be addressed in order to assess the role of blobs in edge plasma transport. For example, if we go beyond reduced models to turbulence simulations, will the physical picture of coherent motion of blobs and the available scalings from the analytic models hold? What fraction of the turbulent flux is due to blob transport rather than other

turbulent processes? How important is 3D physics in determining the blob generation and transport? What aspects of the transport are universal, e.g. independent of the nature of the driving instability and of the particular magnetic geometry?

Thus far, we are aware of just a few examples of 3D simulations of the dynamics of the blobs seeded in background plasma. Simulations [22] were performed with the BOUT fluid turbulence code for DIII-D and NSTX geometry (see also [80]), and another simulation [81] was done recently with the PIC code for a slab geometry with straight magnetic field lines going through “divertor plates” and with the strength varying in the “radial” direction. It was demonstrated that blobs seem to be structurally stable and propagate toward low magnetic field with the speed $\sim 0.1 \times c_s$, which is in reasonable agreement with both analytic estimates and 2D modeling. In the BOUT simulations of coherent filamentary structures in NSTX, reasonable agreement between code and experiment was obtained for correlation times and frequency spectra. Another 3D BOUT simulation for a DIII-D case studied blob production and ballistic transport as a function of collisionality by including a particle source in a simulation which fully evolved the profiles of n , T and Φ . As time elapsed in the simulation, the plasma became more collisional and strong blob production emerged. An analysis [49] showed that the blobs became electrically disconnected from the sheaths and the scaling of blob speed with blob size was reported. The physics of blob disconnection was later studied with the reduced model described in Sec. 4.1 (see Fig. 13) and turbulence simulations with this reduced model [72] show similar behavior to the earlier BOUT simulations [49]. In [74], 3D BOUT simulations of C-Mod and DIII-D cases studied in more detail the effect of X-point geometry on the structure of the turbulence and the blob velocity (also including divertor-leg blobs). In Fig. 19, turbulent density fluctuations are shown for a BOUT simulation of a C-Mod double-null X-point case [74]. The simulation clearly shows the formation of coherent structures with radial and poloidal auto-correlation lengths comparable to the experimental data. Despite this growing body of simulations, much more work is needed to understand edge turbulence and blob physics in 3D geometry.

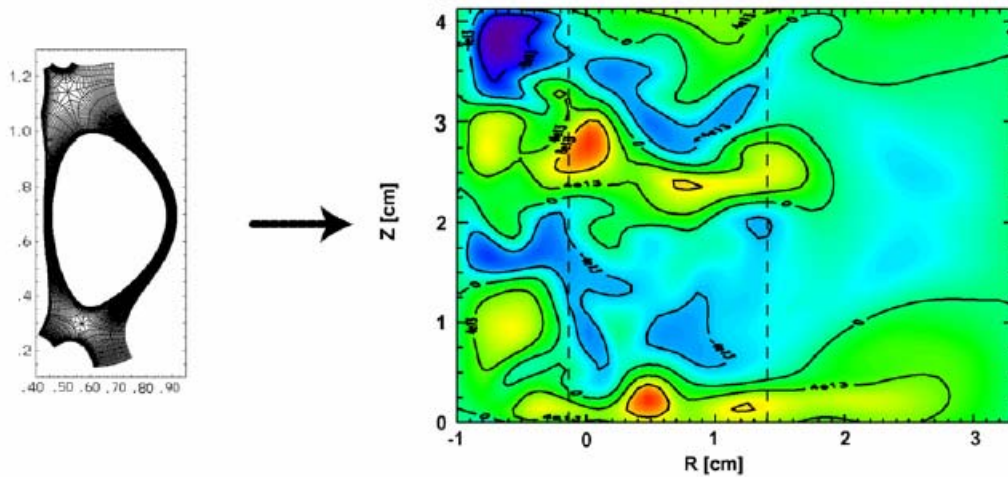


FIG. 19. Density fluctuations at the outer midplane for a BOUT simulation of a C-Mod double-null X-point case. {Taken from Ref. [74]}

Important issues which can be addressed by simulation codes include (i) the relation of blobs to edge plasma turbulence, and (ii) the physics of blob generation. The first results of 2D modeling of SOL plasma turbulence induced by effective gravity were reported about 10-15 years ago (e.g. see Refs. 27, 28 and the references therein). The main focus of these simulations was on statistical properties of the turbulence and comparison with experimental data and theoretical models. It was shown that the probability distribution function (PDF) of the turbulent fluctuations is strongly non-Gaussian with an enhanced fraction of large “events” which ballistically propagate in the radial direction. In Ref. 28 such non-diffusive features were attributed to avalanche-like phenomena. More recent numerical results of 2D modeling of interchange-driven turbulence in the SOL (e.g. see 23, 51,82, and the references therein) largely confirm the strongly non-Gaussian character of the turbulence (see Figs. 20 and 21), but they also observe the formation of blobs and their convective transport toward the wall.

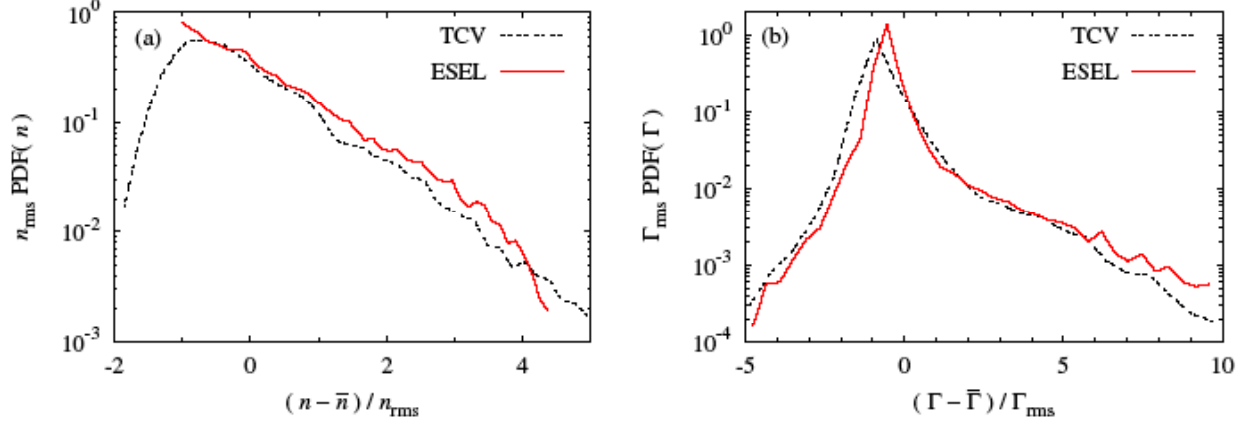


FIG. 20. Rescaled PDFs of (a) the particle density fluctuations and (b) the radial turbulent particle flux at the wall radius for TCV measurements in shots 24530 and 24532 (black dashed curve) and a turbulence simulation matching the SOL conditions (red solid curve) during these probe reciprocations. {Taken from Ref. [23]}

However, as we noted in Sec. 1, good agreement of reduced 2D simulations of plasma turbulence with experimental data may be somewhat superficial. Indeed, only the “bad” curvature region is considered in such simulations, where effective gravity is a key ingredient of the model. The impact of a “good” curvature region or of varying magnetic shear along the field lines due to X-points, which may be crucial for the ballooning type of turbulence, is ignored. These deficiencies, however, do not seem to affect the non-Gaussian PDFs, which tend to be rather generic or “universal” [72, 83, 84]. On the other hand, universality means that these types of diagnostics and comparisons are not a sensitive probe of the underlying physical mechanisms. These points are discussed further below.

The application of 3D edge turbulence codes (e.g. see Refs. 49, 82, 85 and the references therein), which have more complete physics, can address the issues of the validation of blob theory, blob formation mechanisms, comparison with experimental data, etc. However, all of these require a substantial amount of extra work and as of today only a rather crude comparison between simulation and experiment has been made (e.g. see Ref. [5]). In particular, 3D simulations seem to agree with experiments on large fluctuation amplitudes (e.g. $\delta n/n \sim 1$) and a very strong intermittency of the edge plasma turbulence. The resulting effective plasma transport

tends to increase with the increase of plasma density (collisionality) and is higher further out from the separatrix. These features seem to be in a qualitative agreement with the paradigm of blobby transport, but unfortunately, as noted above, there has been little detailed comparison between theoretical models and the results of 3D simulations.

Finally, we discuss possible mechanisms of blob generation. The rate of blob generation cannot be estimated by analytic models, but can only be studied by turbulence simulation codes. Thus, this topic has very important implications for edge plasma transport in general, and so far very little is understood. Important questions include: How and where are blobs formed? Why is blob formation seemingly universal (occurs for different underlying instabilities and in different geometries)? What controls the rate of blob generation (poloidal velocity shear, magnetic geometry, collisionality)?

At an intuitive level, some insight has been obtained. Both experimental data and simulations are consistent with the picture that density blobs arise from the nonlinear saturation of linear instabilities at the plasma edge. For example, curvature-driven interchange drift waves and ballooning modes all tend to arise near the maximum of the linear growth rate, or equivalently, of $|d(\ln n)/dx|$, which defines the “formation zone” of the blobs. The small initial positive and negative density perturbations of the interchange mode both grow and eventually disconnect as part of the turbulent saturation process, forming approximately equal numbers of blobs and holes, respectively. The formation zone is thus characterized statistically by the radial location where the skewness S (third moment of the fluctuations) vanishes, i.e. $S = 0$. The charge polarization induced by curvature (effective gravity) causes the newly-formed coherent objects to move: the enhanced-density blobs move outwards (down the density gradient) and the reduced-density holes move inwards (up the density gradient). This picture has been supported by recent simulations [72] and experiments [65, 86].

A similar picture could be constructed for ELMs in H-mode discharges in tokamaks. The generation of ELMs is typically attributed to peeling-ballooning instabilities, which result in a strong plasma filamentation and transport at the outer side of the torus (see Refs. 87-89 and the

references therein). The maximum peeling-ballooning growth rate occurs near the separatrix where the edge pressure and current gradients are large. Thus, the nonlinear formation of ELM filaments should occur in the vicinity of the separatrix. The observed outwards propagation of the ELM filaments to the wall occurs by the same curvature-driven polarization mechanism as for blobs, the only difference being in the parallel current closure scheme, as discussed in Secs. 2.2 and 4.2.

Thus, the picture just described may explain why blobs and ELM filaments reveal striking similarities. It suggests that the mechanism of the convection of meso-scale structures at the outer side of the torus due to plasma polarization (caused by magnetic field curvature or other outwards forces) and subsequent $\mathbf{E} \times \mathbf{B}$ radial drift is rather universal. Similar transport occurs in many different plasma configurations, both toroidal and linear [84]. As another example, recent data from tokamaks with limiters [90, 91] has clearly demonstrated that edge plasma transport at the outer side of the torus looks very similar in both diverter and limiter configurations. In fact, this statement can be made quantitative: in both experiments [83, 84, 92] and simulations [72], it has been shown that the rescaled PDF of the turbulent fluctuations in the far SOL is nearly identical in all cases [see Fig. 21]. For example, in Ref. [72] it was shown that the rescaled PDF was insensitive to the presence of X-point geometry and to the collisionality of the plasma. This insensitivity of the PDF of the turbulent fluctuations to configuration and parameters suggests that the mechanism underlying the convective transport is the same in all cases.

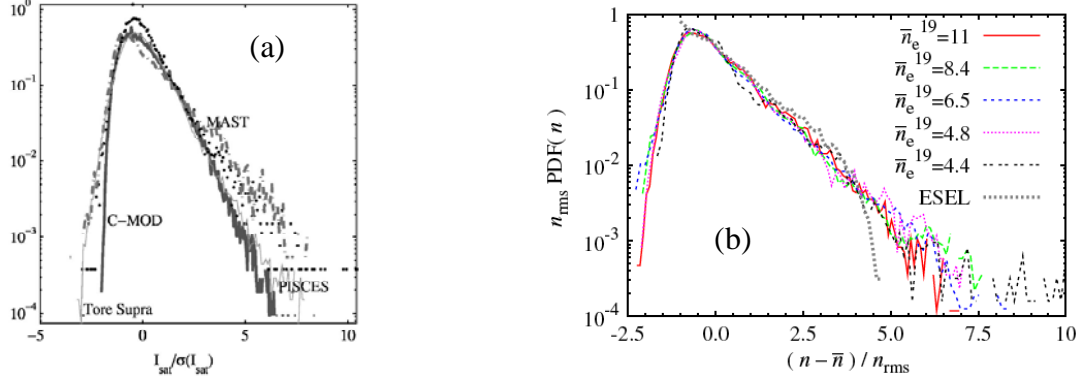


FIG. 21. Rescaled PDFs of (a) the ion saturation current (normalized to the standard deviation) on four machines (C-Mod, Tore-Supra, MAST, and PISCES) {taken from Ref. [84]}; (b) the normalized particle density fluctuations at the wall radius, $(n - \bar{n}) / n_{\text{rms}}$, for varying densities for the TCV tokamak. Also shown is the ESEL code simulation result (grey dashed curve). Note the similar shape of the curve in each case. {Taken from Ref. [83]}

Despite this evolving picture, the details of plasma filamentation and blob formation are not yet fully understood. For example, we note that in the L-mode regime for circular limited tokamaks where X-point and resistive effects can be neglected, the edge plasma is considered to be *stable* with respect to the interchange drive due to stabilization by the good curvature region and the magnetic field line bending (Alfvén waves) as well as ion finite Larmor radius effects. Nevertheless, even in this limit, the interchange drive at the outer side of the torus in the vicinity of the separatrix can play a crucial role in blob generation. The observed similarity of edge turbulence in limited and diverted geometries motivates a search for universal mechanisms.

In [93] it was suggested that the interplay of the interchange drive and nonlinear effects associated with drift wave turbulence (which is rather strong at the edge in L-mode) can lead to the blob formation at the outer side of the torus. It is important to note a vital distinction between the ballooning-type instability considered in Ref. [93] and the structure of the modes in conventional ballooning mode theory. In standard ballooning mode stability analysis, background plasma parameters are considered to be the functions of the magnetic flux surfaces and the structure of the mode is determined by the ballooning equation. In [93] the background

plasma parameters are fluctuating due to drift turbulence. These fluctuations are driven by the instabilities that occur at short cross-field length scale (of the order of the ion gyro-radius) and extend to longer length scales due to inverse cascade. Therefore, Ref. [93] considered a ballooning-type instability of the plasma with parameters which are inhomogeneous in both parallel and cross-field directions. Such an approach is legitimate when the time-scale of the instability is shorter than the characteristic life-time of these plasma structures (limited by e.g. density/pressure equilibration along the magnetic field lines). The scalings found in [93] are in qualitative agreement with experimental observations. Obviously, more work is needed to understand the physics of blob generation and to benchmark theoretical predictions against numerical simulations and experiment.

6.2 Other transport issues

6.2.1 Energy, momentum and current transport

In addition to particles, blobs also carry energy, momentum and currents. This review paper has emphasized the transport of particles, although we touched briefly on energy transport as a mechanism for blob spin, and the transport of parallel current in discussing ELM-filaments. Here, we also mention some work on the other transport issues.

One study used the two-region model to study the effect of blob transport on the thermal equilibrium of the SOL [94]. It was shown that perpendicular heat transport by blobs in the resistive-X-point (RX) regime (assuming X-point diverted geometry) could lead to a thermal collapse of the SOL plasma at high collisionality. This effect is similar to an X-point MARFE with the cooling mechanism of radiation replaced by blob heat convection. The theory predicts an equilibrium bifurcation and a “catastrophe” (root merger leading to an equilibrium limit) at high SOL collisionality when $Q_{\perp} > Q_{\parallel}$. This behavior is consistent with what is observed on C-Mod near the density limit [95], and is also consistent with code results [85, 96, 97] predicting a large increase in turbulent transport at high collisionality.

Some work has also been carried out to study the turbulent transport of momentum, including the effects of blobs [98]. The 2D turbulence simulation included the effects of both curvature-drive and drift-wave physics on the edge and SOL turbulence. A subtle interplay is observed between the turbulent formation of edge shear layers, the blob production, and the momentum transport. The generation of sheared (zonal) flows by drift-wave turbulence is by now part of the standard paradigm [99]. Edge simulations containing drift-wave and curvature (gravity) physics also generate zonal flows [100, 101]. In addition to regulation of the turbulence, at the edge the sheaths provide a sink for momentum. Consequently, turbulent (e.g. blob) losses at the edge result in a back-reaction that can induce rotation in the core plasma [70]. We note in this regard that the often employed Boussinesque approximation is inadequate because it violates momentum conservation.

Finally, as discussed in Sec 4.2, when sufficiently hot, the ELM-blob filaments can also carry a “monopole” distribution of parallel current [70] (in addition to the dipole polarization-induced current described in Sec. 2), leaving behind a current hole. This process may be very relevant in the H-mode, where relaxation of the edge parallel current in the hot pedestal occurs through ELM transport, and the ELM filaments are observed to act like blobs in the SOL. The monopole current adds additional dynamics to the blob motion through the magnetic force between two currents, which has been recently studied analytically [70].

6.2.2 Drift-wave “blobs”

As shown in Secs. 1 and 2, ballistic propagation of blobs in conventional blob theory [16, 17] arises from the polarization charges induced by an external force (often represented as an “effective gravity”). The dipole pattern of polarization charges also forms a potential and vorticity dipole (see Fig. 5). However, a potential dipole pattern can be driven in a turbulent fluid, just by the random correlation of fluctuations. This process can be expected to occur even when effective gravity is totally absent, e.g. in pure drift-wave turbulence. Transient dipoles formed at the plasma edge due to such turbulence, would then also convect radially outwards by

an $\mathbf{E} \times \mathbf{B}$ drift. The question arises as to how deeply such transient “blobs” would penetrate into the SOL relative to gravity-driven blobs, for which the charge polarization is continuously being refreshed.

The time history for the decaying potential in the SOL region is described by the vorticity equation, Eq. (13), omitting the gravity term. As a result, balancing vorticity advection with parallel current loss to the sheaths we find the estimate of the radial penetration depth L_{pen} of such transient blobs as

$$\left(\frac{L_{\text{pen}}}{L_{\parallel}} \right)_{\text{transient}} \sim \frac{e\Phi_0}{T_e} \left(\frac{\rho_s}{\delta_b} \right)^3. \quad (31)$$

where Φ_0 is the magnitude of the induced potential dipole and the ordering $L_x = L_{\text{pen}} > L_y \sim \delta_b$ was used. On the other hand, the penetration depth of the blobs driven in the SOL by gravity can be estimated (in the sheath connected regime) as

$$\left(\frac{L_{\text{pen}}}{L_{\parallel}} \right)_{\text{gravity}} \sim \frac{L_{\parallel}}{R} \left(\frac{\rho_s}{\delta_b} \right)^2. \quad (32)$$

Here, the estimate $L_{\text{pen}} \sim V_b \tau_{\parallel}$ was used with the radial blob velocity V_b given by Eq. (16) and the lifetime of the blob estimated from particle loss as $\tau_{\parallel} \sim L_{\parallel} / c_s$. Comparing expressions (31) and (32) for $e\Phi_0 / T < 1$, $\rho_s / \delta_b < 1$, and $L_{\parallel} / R > 1$ we find that gravity-driven blobs penetrate much deeper into the SOL.

However, these transient dipoles may actually result in the formation of gravity-driven blobs in the regions where the effective gravity would “help” to propel dipoles further from the place of origin (e.g. at the outer side of the tokamak).

6.2.3 Quantitative transport calculations

Although 3D codes can be used to simulate edge plasma turbulence, the simulation of the edge plasma on transport time-scales with all the complexity of neutral transport and plasma-neutral interactions, impurity, atomic physics, plasma-wall interactions, etc., is beyond their

capabilities. Therefore, for such purposes 2D edge plasma transport codes (e.g. UEDGE [102], SOLPS [103]) are used. In these codes, anomalous cross-field plasma transport is usually described by adding diffusive terms into the particle and energy balance equations. Corresponding diffusion coefficients are taken either from some analytic/numerical models or, in most cases, simply by fitting experimental data.

However, application of diffusive models for the study of plasma transport in the far SOL and for plasma-wall interactions shows that only extremely large diffusion coefficients (\sim a few $10 \text{ m}^2/\text{s}$) can fit basic experimental data. As a result, it is impossible to identify any physics-based diffusion process associated with such transport. Therefore, in Ref. [104] it was suggested that a diffusion-convective model be used, where the outward radial convective velocity, V_c , is strongly inhomogeneous in the poloidal direction and is peaked at the outer side of the torus in agreement with the paradigm of blobby plasma transport.

Such an approach immediately resolved the issue of otherwise needing unphysically large diffusion coefficients, and it allowed the comparison of transport coefficients (e.g. convective velocity) with physics-based models of edge plasma turbulence and blob dynamics. In particular, it was demonstrated in Refs. [105, 106] that in order to fit experimental data the convective velocity of impurity ions in the far SOL should depend on the ionization charge. For example, while fully-stripped Carbon ions should be convected toward the wall, singly-ionized Carbon ions should be convected toward the core. And, as a matter of fact, this feature of impurity transport has a very clear relation to the convection of blobs and holes in opposite directions, which was discussed in Sec. 3. Blobs carry fully-stripped impurities from the hot plasma in the vicinity of the separatrix to the wall, whereas holes carry relatively low-temperature plasma and freshly ionized impurity atoms spattered from the wall towards the hotter edge plasma. Since the hole plasma temperature is low, and blob and hole plasmas do not interact much, freshly-ionized impurity ions remain in low ionization states while being convected by the holes (see Refs. [105, 106] for details). We point out that the convection of impurities from the wall toward the

separatrix may have very important consequences for core plasma performance and should be studied more intensively especially in the content of impurity accumulation in tokamak reactor.

Another interesting feature coming from edge plasma simulations with the diffusion-convection model (and one which can bridge theory, experiment, and edge plasma transport simulation) is the magnitude of the radial velocity of hydrogenic species needed to fit experimental data. It appears that the velocity $V_c \sim 50-100$ m/s is enough [104] to fit the data, while theoretical estimates and modeling give $V_b \sim 500-1000$ m/s as the typical velocity of a single blob. As a matter of fact, this rather low magnitude of V_c is very much what should be expected, and the reason for the difference between the magnitudes of V_c and V_b can be perfectly explained by the paradigm of intermittent blobby transport. The issue is that 2D edge plasma transport codes are dealing with averaged plasma parameters, e.g. velocity V_c and, in particular, with the average density $\langle n \rangle$, which is usually 2-3 times smaller than blob plasma density n_b . Moreover, according to experiment the ~~dwelling-time~~ waiting time between two consecutive blobs arriving at some point in SOL is much larger than the time duration of the blob itself passing the given point, by a factor $C \sim 10-30$. Therefore, the averaged plasma flux is $V_c \langle n \rangle$ from the point of view of averaged plasma parameters used in 2D transport codes, while in terms of blob parameters it can be written as $V_b n_b / C$. As a result we find that $V_c = V_b n_b / (C \langle n \rangle) \sim 0.1 \times V_b$, in agreement with Ref. [104].

The latter example raises the important, and not quite resolved, problem of the simulation of edge plasma transport and other nonlinear processes in 2D codes based on averaged plasma parameters, while these parameters actually experience very strong fluctuations. The fundamental problem is that $\langle f(Q) \rangle \neq f(\langle Q \rangle)$, where f is a nonlinear function representing, for example, blob convection, neutral ionization and radiation, wall physics (sputtering, recycling), etc., Q is a variable such as density or temperature, and $\langle \dots \rangle$ is a fast-time-scale and toroidal average. It is not straightforward to obtain a “closure” procedure which expresses $\langle f(Q) \rangle$ in terms of the variables $\langle Q \rangle$ evolved by the transport code. Thus the contribution of blobs and intermittent objects to these processes is difficult to describe in transport equations.

6.2.4 Similarity of edge mesoscale structures and pellet clouds

In addition to such mesoscale structures as blobs and ELMs, high-density pellet clouds used for core fueling also convect radially by a similar curvature-driven polarization mechanism. Whereas blobs and ELMs naturally occur on the low field side of a toroidal machine in the vicinity of the separatrix and propagate into the SOL, pellet clouds are formed as a result of pellet ablation after the pellets are injected relatively deep into the core plasma.

When pellets penetrate into relatively hot plasma, the energy flux onto the pellet increases and the pellet starts to ablate, spreading around a cloud of gas/plasma. This cloud somewhat screens the pellet from the energy flux and fast ablation and helps in the further propagation of the pellet. The physics of ablation and screening is rather complex and the details can be found in Ref. [107]. Here, we will only discuss the dynamics of clouds and its similarity with that of blobs and ELMs.

First, we notice that the plasma density in the cloud is much higher than that in surrounding plasma. Then due to fast heating of the cloud, caused by the parallel electron heat flux, the pressure in the cloud becomes large. As a result, the cloud starts to expand along the magnetic field lines, forming a high pressure/density filament rather similar to the filaments of blobs and ELMs. Obviously the dynamics of the cloud filament plays an important role in the screening of the pellet and, hence, in the ablation process and penetration depth of the pellet. In Refs. [108-110] it was shown that, similar to blobs and ELMs, the cross-field polarization of a high pressure/density filament due to the drag force, and most importantly by magnetic field inhomogeneity, causes an $\mathbf{E} \times \mathbf{B}$ drift of the cloud with respect to the pellet, which reduces pellet screening.

Because pellet ablation and the formation of the cloud occur mainly on closed flux surfaces, closure of the cross-field polarization current in the parallel direction is based either on resistive effects [108] or on the bending of magnetic field lines [109]. In this respect the equations describing the evolution of clouds are rather similar to that describing blob dynamics

in resistive and “high beta” regimes. The results of numerical simulation of cloud $\mathbf{E} \times \mathbf{B}$ drifts with respect to the pellet are shown in Fig. 22 taken from Ref. [110]. The source of plasma, which mocks up the ablation of the pellet, is localized in Fig. 22 in the vicinity of $x = y = 0$. The formation of the “mushroom-like” shape of the plasma density contours looks similar to that of blobs in some particular regimes.

The pronounced effect of the outward drift of the pellet cloud was proposed as a likely explanation of the relatively low efficiency of the fueling of tokamak plasmas by injecting of pellets from the low magnetic field side [111]. Such an interpretation was supported by both video observations and by investigation of ablation dynamics at high temporal resolution (see also Ref. [112]).

These findings led to the natural suggestion that one could improve the fueling efficiency of a tokamak plasma with pellets by injecting pellets from high magnetic field side. The argument was that in this case the polarization of the ablation cloud and corresponding $\mathbf{E} \times \mathbf{B}$ drift will advect the cloud plasma towards the core, in contrast to low magnetic field side injection, where $\mathbf{E} \times \mathbf{B}$ drift advects cloud plasma away from the core. Experimental data from Ref. [113], where pellet injection in ASDEX plasma was performed from the high magnetic field side showed improved fueling efficiency and favorable motion of the ablation cloud in support of this idea. Theoretical analysis of pellet injection from high magnetic field side can be found in Ref. [114].

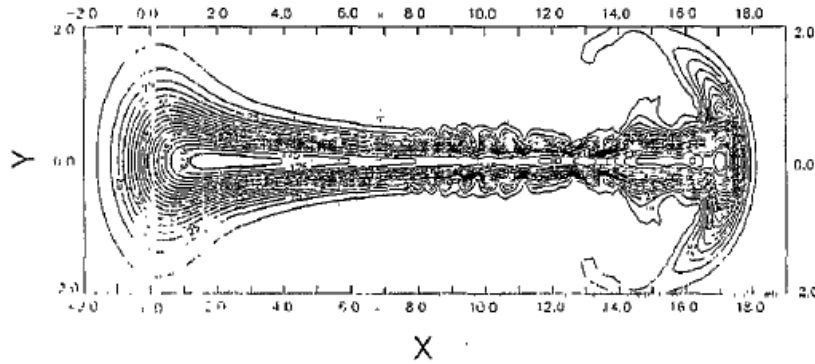


FIG. 22. The cloud plasma density contours at some time after “ablation” starts. {Taken from Ref. [110].}

7. Summary and Conclusions

In this paper, we have reviewed some theoretical aspects of the dynamics of the meso-scale filaments extending along the magnetic field lines in the edge plasma, which are often called “blobs”. In Secs. 1 and 2, after a brief historical survey of experimental data, we presented the main ideas on edge and SOL plasma transport, which finally evolved into the modern paradigm of convective, very intermittent, cross-field edge plasma transport.

In Secs. 3 and 4, we showed that both analytic theory and numerical simulations demonstrate that plasma blobs with enhanced pressure can be coherently convected toward the wall. The mechanism of convection is related to an effective gravity force (e.g. due to magnetic curvature effects), which causes plasma polarization and a corresponding $\mathbf{E} \times \mathbf{B}$ convection. Theory and simulation predict blob propagation speeds of the order of a few hundred meters per second and cross-field sizes of the order of a centimeter for both current tokamaks and in ITER. These predictions, as well as the shape of plasma density profile in the blob (sharp front with a long tail), are in reasonable agreement with available experimental data. Moreover, the concept of blobs as a fundamental entity of convective transport in the SOL provides explanations for the observed outwards convective transport, intermittency and non-Gaussian statistics in edge plasmas, and enhanced wall recycling in both toroidal and linear machines.

In Sec. 5, we presented the results of both the study of structural stability of blobs and the analyses of the impacts of different effects (e.g. X-point magnetic geometry, plasma collisionality, plasma beta, etc.) on blob dynamics and discuss governing dimensionless parameters. A “blob correspondence principle” is described, which allows blob velocity scalings to be obtained from linear stability theory. The scalings of blob speed with respect to the cross-field size of the blobs (found for different leading dimensionless parameters) are compared with experimental observations giving some idea of the regimes of blob propagation in the experiment.

Finally, in Sec. 6 we briefly discussed a number of related topics: the main features of edge and SOL plasma turbulence including ELMs, the results of 2D and 3D edge turbulence simulations, possible mechanisms of blob generation, and the implications for edge and SOL plasma macroscopic transport. While the physics of blob propagation is much better understood than the mechanism(s) of blob generation, some progress on the latter topic was discussed. In Sec. 6.1 two physical pictures were considered: one in which the linear interchange-ballooning mode is unstable and a nonlinear saturation mechanism produces the blobs at the location of the maximum linear growth rate, and a second picture in which nonlinear effects are necessary for the instability. Further work is needed to understand the domain of applicability of these models, and how the blob formation process interacts with sheared flows.

Another area for future work is the generalization of the MHD fluid models discussed here to include kinetic effects. One example is the PIC simulation of blob transport discussed in Sec. 6.1. General-purpose edge kinetic codes using both PIC and Vlasov-fluid methods are being developed world-wide and will be useful for studying kinetic effects on blobs. Effects which are expected to be important include finite ion temperature (e.g. in the far SOL where $T_i \gg T_e$ pertains, especially for ELMs) and finite ion Larmor radius (for $\delta_b \sim \rho_i$), and the role of electron kinetic effects and non-Maxwellian tails on parallel thermal and electrical conductivity, and on the sheath closure relations (when the Braginskii condition $L_{\parallel} \gg \lambda_{ei}$ is violated).

Our understanding of the topics discussed in this review is rapidly evolving through the combined efforts of many researchers, and we expect that progress in this field will be rapid in the next several years.

Acknowledgments

This work was supported by the U.S. Department of Energy (DOE) under DOE Grants No. DE-FG02-04ER54739 and DE-FG02-97ER54392.

References

- [1] ITER Physics Basis, Chapter 4: Power and particle control, (1999) *Nucl. Fusion* **39**, 2391.
- [2] Krasheninnikov, S. I. , Pigarov, A. Yu., Knoll, D. A., et al., (1997) *Phys. Plasmas* **4**, 1638.
- [3] Goodall, D. H. J., (1982) *J. Nucl. Materials* **111 & 112**, 11.
- [4] Zweben, S. J., (1985) *Phys. Fluids* **28**, 974.
- [5] Terry, J. L., Zweben, S. J., Hallatschek, K., LaBombard, B., Maqueda, R. J., et al., (2003) *Phys. Plasmas* **10**, 1739.
- [6] Liewer, P. C., (1985) *Nucl. Fusion* **25**, 543.
- [7] Wootton, A. J., Carreras, B. A., Matsumoto, H., et al., (1990) *Phys. Fluids B* **2**, 2879.
- [8] Endler, M., (1999) *J. Nucl. Mater.* **266-269**, 84.
- [9] Hidalgo, C., (1995) *Plasma Phys. Control. Fusion*, **37**, A53.
- [10] Neuhauser, J., Bessenrodt-Weberpals, M., Braams, B.J., et al., (1989) *Plasma Phys. Control. Fusion*, **31**, 1551.
- [11] Matthews, G. F., (1995) *J. Nucl. Mater.* **220-222**, 104.
- [12] Asakura, N., Koide, Y., Itami, K., *J. Nucl. Mater.* (1995) **220-222**, 104.
- [13] Umansky, M. V., Krasheninnikov, S. I., LaBombard, B., Terry, J. L., (1998) *Phys. Plasmas* **5**, 3373.
- [14] Krasheninnikov, S. I., (1998) *Czechoslovak J. of Phys.* **48**, Suppl. S2, 97.
- [15] Rudakov, D. L., Boedo, J. A., Moyer, R. A., et al., (2002) *Plasma Physics and Controlled Fusion* **44**, 717.
- [16] Krasheninnikov, S. I., (2001) *Phys. Lett. A* **283**, 368.
- [17] D'Ippolito, D. A., Myra, J. R., and Krasheninnikov, S. I., (2002) *S. I., Phys. Plasmas* **9**, 222.
- [18] Kunkel, W. B., and Guillory, J. U., (1965) in *Proceedings of the Seventh Conference on Phenomena in Ionized Gases*, Belgrade, edited by B. Perovic and D. Tocsic (Gradjevinska Knjiga, Belgrade, Yugoslavia, 1966), **Vol. II**, p. 702
- [19] Kadomtsev, B. B., (1965) in *Proceedings of the Seventh Conference on Phenomena in Ionized Gases*, Belgrade, edited by B. Perovic and D. Tocsic (Gradjevinska Knjiga,

Belgrade, Yugoslavia, 1966), **Vol. II**, p. 610

- [20] D'Ippolito, D. A., Myra, J. R., Krasheninnikov, S. I., Yu, G. Q., and Pigarov, A. Yu, (2004) *Contrib. Plasma Phys.* **44**, 205.
- [21] Krasheninnikov, S. I., Smolyakov, A. I., Yu, G. and Soboleva, T. K., (2005) *Czech. J. of Phys.* **55**, 307.
- [22] Krasheninnikov, S. I., Pigarov, A. Yu., Galkin, S. A., et al., (2002) in *Proceedings of the 19th IAEA Fusion Energy Conference*, Lyon, France (International Atomic Energy Agency, Vienna, 2003), paper IAEA-CN-94/TH/4-1.
- [23] Garcia, O. E., Horacek, J., Pitts, R. A., Nielsen, A. H., Fundamenski, W., Graves, J. P., Naulin, V., and Rasmussen, J. J., (2006) *Plasma Phys. Control. Fusion* **48**, L1-L10.
- [24] Myra, J. R., D'Ippolito, D. A., Stotler, D. P., Zweben, S. J., LeBlanc, B. P., Menard, J. E., Maqueda, R. J., and Boedo, J., (2006) *Phys. Plasmas* **13**, 092509.
- [25] Nedospasov, A. V., (1989) *Sov. J. Plasma Phys.* **15**, 659.
- [26] Garbet, X., Laurent, L., Roubin, J.-P. and Samain, A., (1991) *Nucl. Fusion* **31**, 967;
- [27] Benkadda, S., Garbet, X., and Verga, A., (1994) *Contrib. Plasma Phys.* **34**, 247; Benkadda, S., Dudok de Wit, T., Vegra, A., et al., (1994) *Phys. Rev. Lett.* **73**, 3403
- [28] Sarazin, Y. , and Ghendrih, Ph., (1998) *Phys. Plasmas* **5**, 4214.
- [29] Bak, P., Tang, C., and Wiesenfeld, K., (1987) *Phys. Rev. Lett.* **59**, 381.
- [30] Diamond, P. H. and Hahm, T. S., (1995) *Phys. Plasmas* **2**, 3640.
- [31] Newman, D. E., Carreras, B. A., Diamond, P. H. and Hahm, T. S., (1996) *Phys. Plasmas* **3**, 1858.
- [32] Rozhansky, V., Veselova, I. and Voskoboynikov, S., (1995) *Plasma Phys. Control. Fusion* **37**, 399.
- [33] Parks, P. B., Sessions, W. D. and Baylor, L. R., (2000) *Phys. Plasmas* **7**, 1968.
- [34] Carreras, B. A., (2005) *J. Nucl. Mater.* **337-339**, 315.
- [35] Zweben, S.J., Boedo, J.A., Grulke, O., Hidalgo, C., LaBombard, B., Maqueda, R.J., Scarin, P., and Terry, J.L., (2007) *Plasma Phys. Control. Fusion* **49**, S1.
- [36] Cohen, R. H., and Ryutov, D. D., (2006) *Contrib. Plasma Phys.* **46**, 678.
- [37] Krasheninnikov, S. I., and Smolyakov, A. I., (2003) *Phys. Plasmas* **10**, 3020.

- [38] Krasheninnikov, S.I., Smolyakov, A. I., and Soboleva, T. K., (2005) *Phys. Plasmas* **12**, 072502.
- [39] Ryutov, D. D., (2006) *Phys. Plasmas* **13**, 122307.
- [40] Myra, J. R., Boedo, J., Coppi, B., D'Ippolito, D.A., Krasheninnikov, S.I., LeBlanc, B.P., Lontano, M., Maqueda, R., Russell, D.A., Stotler, D.P., Varischetti, M.C., Zweben, S.J., and the NSTX Team, (2007) in *Plasma Physics and Controlled Nuclear Fusion Research 2006* (IAEA, Vienna, 2007), paper IAEA-CN-149-TH/P6-21.
- [41] Yu, G. Q., Krasheninnikov, S. I., Guzdar, P. N., (2006) *Phys. Plasmas* **13**, 042508.
- [42] Myra, J. R., D'Ippolito, D. A., Krasheninnikov, S. I., and Yu, G. Q., (2004) *Phys. Plasmas* **11**, 4267.
- [43] Berk, H., Ryutov, D.D., and Tsidulko, Yu A., (1990) *JETP Lett.* **52**, 23.
- [44] Krasheninnikov, S. I., Ryutov, D. D., and Yu, G., (2004) *J. Plasma Fusion Res.* **6**, 139.
- [45] Myra, J. R., and D'Ippolito, D. A., (2005) *Phys. Plasmas* **12**, 092511.
- [46] Myra, J. R., Russell, D. A., and D'Ippolito, D. A., (2006) *Phys. Plasmas* **13**, 112502.
- [47] Farina, D., Pozzoli, R., Ryutov, D. D., (1993) *Nucl. Fusion* **33**, 1315.
- [48] Ryutov, D. D., and Cohen, R. H., (2004) *Contrib. Plasma Phys.* **44**, 168.
- [49] Russell, D. A., D'Ippolito, D. A., Myra, J. R., Nevins, W. M., and Xu, X. Q., (2004) *Phys. Rev. Lett.* **93**, 265001.
- [50] Garcia, O. E., Bian, N. H., Naulin, V, Nielsen, A. H. Nielsen, and Rasmussen, J.J., (2005) *Phys. Plasmas* **12**, 090701.
- [51] Fundamenski, W., Garcia, O. E., Naulin, V., Pitts, R. A., et al., (2007) *Nucl. Fusion* **47**, 417.
- [52] Garcia, O., Naulin, V., Nielsen, A. H., and Rasmussen, J. J., (2005) *Phys. Plasmas* **12**, 062309.
- [53] Garcia, O., Bian, N. H., Fundamenski, W., (2006) *Phys. Plasmas* **13**, 082309.
- [54] Bian, N., Benkadda, S., Paulsen, J.-V, and Garcia, O. E., (2003) *Phys. Plasmas* **10**, 671.
- [55] D'Ippolito, D. A., and Myra, J. R., (2003) *Phys. Plasmas* **10**, 4029.
- [56] Yu, G. Q., and Krasheninnikov, S. I., (2003) *Phys. Plasmas* **10**, 4413.
- [57] Aydemir, A. Y., (2005) *Phys. Plasmas* **12** 62503.

- [58] Garcia, O., Bian, N. H., Fundamenski, W., (2006) *Phys. Plasmas* **13**, 082309.
- [59] Tomkins, C., Prestridge, K., Rightley, P., et al., (2003) *Phys. Fluids* **15**, 986.
- [60] Sudan, R. N., Gruzinov, A. V., Horton, W., and Kukharkin, N., (1997) *Phys. Rep.* **283**, 95.
- [61] Rudakov, D. L., Boedo, J. A., Moyer, R. A., et al., (2005) *Nucl. Fusion* **45**, 1589.
- [62] Carter, T. A., (2006) *Phys. Plasmas* **13**, 10701.
- [63] Rudakov, D. L., Boedo, J. A., Moyer, R. A., et al., (2005) *Nucl. Fusion* **45**, 1589.
- [64] Carter, T. A., (2006) *Phys. Plasmas* **13**, 10701.
- [65] Boedo, J. A., Rudakov, D. L., Moyer, R. A., et al., (2003) *Phys. Plasmas* **10**, 1670.
- [66] D'Ippolito, D. A., Myra, J. R., Russell, D. A., and Yu, G. Q., (2004) *Phys. Plasmas* **11**, 4603.
- [67] Myra, J. R., D'Ippolito, D. A., Xu, X.Q., and Cohen, R.H., (2000) *Phys. Plasmas* **7**, 2290.
- [68] Myra, J. R., D'Ippolito, D. A., Xu, X.Q., and Cohen, R.H., (2000) *Phys. Plasmas* **7**, 4622.
- [69] Xu, X. Q., Cohen, R. H., Rognlien, T. D., and Myra, J.R., (2000) *Phys. Plasmas* **7**, 1951.
- [70] Myra, J. R., (2007) "Current carrying blob-filaments and ELM dynamics," Lodestar Report LRC-07-116, (2007) to be published in *Phys. Plasmas*.
- [71] Umansky, M. V., Rognlien, T. D., Xu, X. Q., Cohen, R. H., and Nevins, W. M., (2004) *Contrib. Plasma Phys.* **44**, 182.
- [72] Russell, D. A., Myra, J. R., D'Ippolito, D. A., (2007) *Phys. Plasmas* **14**, 102307.
- [73] Cohen, R.H., LaBombard, B., LoDestro, L.L., Rognlien, T.D., Ryutov, D.D., Terry, J.L., Umansky, M.V., Xu, X.Q., Zweben, S., (2006) "Fluid Simulations and Theory of Boundary Plasma Fluctuations," in *Plasma Physics and Controlled Nuclear Fusion Research 2006* (IAEA, Vienna, 2007), paper IAEA-CN-149-TH/P6-25.
- [74] Cohen, R.H., LaBombard, B., Ryutov, D.D., Terry, J. L., Umansky, M.V., Xu, X.Q., and Zweben, S., (2007) *Nucl. Fusion* **47**, 612.
- [75] Cohen, R.H., and Ryutov, D.D., (2005) *Plasma Phys. Control. Fusion* **47**, 1187.
- [76] Endler, M., Niedermeyer, H., Giannone, L., Holzhauser, E., Rudyj, A., Theimer, G., Tsois, N. and the ASDEX Team, (1995) *Nucl. Fusion* **35**, 1307.
- [77] Garcia, O. E., Bian, N. H., Naulin, V, Nielsen, A. H. Nielsen, and Rasmussen, J. J., (2005)

Phys. Plasmas **12**, 090701.

- [78] Grulke, O., Terry, J.L., LaBombard, B., and Zweben, S.J., (2006) *Phys. Plasmas* **13**, 012306.
- [79] Zweben, S.J., Maqueda, R. J., Terry, J. L., Munsat, T., Myra, J. R., D'Ippolito, D.A., Russell, D. A., et al., (2006) *Phys. Plasmas* **13**, 056114.
- [80] Xu, X. Q., Nevins, W. M., Cohen, R. H., Myra, J. R., and Snyder, P. B., (2002) *New J. Phys.* **4**, 53.
- [81] Ishiguro, S., Hasegawa, H., (2006) *J. Plasma Phys.* **72**, 1233.
- [82] Scott, B. D., (2007) *Plasma Phys. Control. Fusion* **49**, S25
- [83] Garcia, O. E., Horacek, J., Pitts, R. A., Nielsen, A. H., Fundamenski, W., Naulin V. and Rasmussen, J. J., (2007) *Nucl. Fusion* **47**, 667.
- [84] Antar, G., Counsell, G., Yu, Y., Labombard, B., and Devynck, P., (2003) *Phys. Plasmas* **10**, 419.
- [85] Xu, X. Q., Nevins, W. M., Rognlien, T. D., et al., (2003) *Phys. Plasmas* **10**, 1773.
- [86] Furno, I., Labit, B., Podesta, M., Fasoli, A., Diallo, A., et al., "Mechanism for plasma blob generation from drift-interchange waves," submitted to *Phys. Review Lett.* (2007).
- [87] Connor, J. W., (1998) *Plasma Phys. Controlled Fusion* **40**, 531.
- [88] Wilson, H. R., Cowley, S. C., (2004) *Phys. Rev. Lett.* **92**, 175006.
- [89] Snyder, P. B., Wilson, H. R., Xu, X. Q., (2005) *Phys. Plasmas* **12**, 056115.
- [90] Kirnev, G. S., Budaev, V. P., Grashin, S. A., et al., (2004) *Plasma Phys. Contr. Fusion* **46**, 621.
- [91] Gunn, J. P., Boucher, C., Dionne, M., et al., (2007) *J. Nucl. Mater.* **363–365**, 484.
- [92] Graves, J. P., Horacek, J., Pitts, R. A., and Hopcraft, K. I., *Plasma Phys. Control. Fusion* **47**, L1 (2005).
- [93] Krasheninnikov, S. I., Smolyakov, A. I., "Generation of meso-scale convective structures in tokamak edge plasma", submitted to *Phys. Plasmas*, 2007.
- [94] D'Ippolito, D. A., and Myra, J. R., (2006) *Phys. Plasmas* **13**, 062503.
- [95] LaBombard, B., Hughes, J. W., Mossessian, D., Greenwald, M., Lipshultz, B., Terry, J. L., et al., (2005) *Nucl. Fusion* **45**, 1658.

- [96] Scott, B., (1997) *Plasma Phys. Control. Fusion* **39**, 1635.
- [97] Rogers, B. N., Drake, J. F., and Zeiler, A., (1998) *Phys. Rev. Lett.* **81**, 4396; Rogers, B. N., and Drake, J. F., (1997) *Phys. Rev. Lett.* **79**, 229.
- [98] Myra, J.R., Boedo, J., Coppi, B., D'Ippolito, D.A., Krasheninnikov, S.I., et al., "Blob Transport Models, Experiments, and the Accretion Theory of Spontaneous Rotation," 21st IAEA Fusion Energy Conference, October 16-21, 2006, Chengdu, China, paper TH/P6-21.
- [99] Diamond, P. H., Itoh, S.-I., Itoh, K., and Hahm, T. S., (2005) *Plasma Phys. Control. Fusion* **47**, R35.
- [100] Garcia, O. E., Naulin, V., Nielsen, A. H., and Rasmussen, J. J., (2004) *Phys. Rev. Lett.* **92**, 165003; Garcia, O. E., Bian, N. H., Paulsen, J.-V., Benkadda, S., and Rypdal, K., (2003) *Plasma Phys. Control. Fusion* **45**, 919.
- [101] Bisai, N., Das, A., Deshpande, S., Jha, R., Kaw, P., Sen, A., and Singh, R., (2005) *Phys. Plasmas* **12**, 102515.
- [102] Rognlien, T. D., Milovich, J. L, Rensink, M. E., et al., (1992) *J. Nucl. Mater.* **196–198**, 34.
- [103] Schneider, R., Bonnin, X., Borrass, K., Coster, D. P., Kastelewicz, H., Reiter, D., Rozhansky, V. A., and Braams, B. J., (2006) *Contrib. Plasma Phys.* **46**, 3.
- [104] Pigarov, A. Yu., Krasheninnikov, S. I., Rognlien, T. D., Schaffer, M. J., and West, W. P., (2002) *Phys. Plasmas*, **9**, 1287.
- [105] Pigarov, A. Yu., Krasheninnikov, S. I., Rognlien, T. D., West, W. P., LaBombard, B., Lipschultz, B., Maingi, R., Soukhanovskii, V., (2004) *Contrib. Plasma Physics* **44**, 228.
- [106] Pigarov, A. Yu., Hollmann, E.M., Krasheninnikov, S.I., Rognlien, T.D., and West, W.P., (2005) *J. Nucl. Mater.*, **337-339**, 371.
- [107] Milora, S.L., Houlberg, W.A., Lengyel, L.L. and Mertens, V., (1995) *Nucl. Fusion* **35**, 657.
- [108] Veselova, I. Yu., and Rozhansky, V. A., (1991) *Sov. J. Plasma Phys.* **17**, 817.
- [109] Parks, P. B., (1992) *Nucl. Fusion* **32**, 2137.
- [110] Rozhansky, V., Veselova, I., and Voskoboynikov, S., (1995) *Plasma Phys. Control. Fusion* **37**, 399.
- [111] Lang, T., Zohm, H., Buchl, K., Fuchs, J. C., Gehre, O., Gruber, O., Mertens, V., Muller, H. W., Neuhauser, J., Asdex Upgrade and NBI Teams, (1996) *Nucl. Fusion* **36** 1531.

- [112] Durst, R. D., Rowan, W. I., Austin, M. E., Collins, R. I., Gandy, R. F., Phillips, P. E., Richards, B., (1990) *Nucl. Fusion* **30**, 3.
- [113] Lang, P. T., Buchl, K., Kaufmann, M., Lang, R. S., Mertens, V., Muller, H. W., Neuhauser, J., ASDEX Upgrade and NBI Teams, (1997) *Phys. Rev. Lett.* **79**, 1487.
- [114] Parks, P. B., Sessions, W. D., and Baylor, L. R., (2000) *Phys. Plasmas* **7**, 1968.